# Active gas features in three HSC-SSP CAMIRA clusters revealed by high angular resolution analysis of MUSTANG-2 SZE and XXL X-ray observations⋆

Nobuhiro Okabe[1,2,3]†, Simon Dicker[4], Dominique Eckert[5], Tony Mroczkowski[6], Fabio Gastaldello[7], Yen-Ting Lin[8], Mark Devlin[4], Charles E. Romero[4], Mark Birkinshaw[9], Craig Sarazin[10], Cathy Horellou[11],Tetsu Kitayama[12], Keiichi Umetsu[8], Mauro Sereno[13], Brian S. Mason[14], John A. ZuHone[15], Ayaka Honda[1], Hiroki Akamatsu[16], I-Non Chiu[8], Kotaro Kohno[17,18], Kai-Yang Lin[8], Elinor Medezinski[19], Satoshi Miyazaki[20], Ikuyuki Mitsuishi[21], Atsushi J. Nishizawa[22], Masamune Oguri[23,17,24], Naomi Ota[25], Florian Pacaud[26], Marguerite Pierre[27], Jonathan Sievers[28], Vernesa Smolčić[29], Sara Stanchfield[4], Keigo Tanaka[30], Ryoichi Yamamoto[1], Chong Yang[1], and Atsushi Yoshida[21]

[1]*Department of Physical Science, Hiroshima University, 1-3-1 Kagamiyama, Higashi-Hiroshima, Hiroshima 739-8526, Japan*
[2]*Hiroshima Astrophysical Science Center, Hiroshima University, 1-3-1 Kagamiyama, Higashi-Hiroshima, Hiroshima 739-8526, Japan*
[3]*Core Research for Energetic Universe, Hiroshima University, 1-3-1, Kagamiyama, Higashi-Hiroshima, Hiroshima 739-8526, Japan*
[4]*Department of Physics and Astronomy, University of Pennsylvania, 209 South 33rd Street, Philadelphia, PA, 19104, USA*
[5]*Department of Astronomy, University of Geneva, ch. dEcogia 16, 1290 Versoix, Switzerland*
[6]*ESO - European Southern Observatory, Karl-Schwarzschild-Str. 2, D-85748 Garching b. München, Germany*
[7]*INAF - IASF Milano, via Bassini 15, I-20133 Milano, Italy*
[8]*Academia Sinica Institute of Astronomy and Astrophysics (ASIAA), No. 1, Section 4, Roosevelt Road, Taipei 10617, Taiwan*
[9]*H.H. Wills Physics Laboratory, University of Bristol, Tyndall Avenue, Bristol, BS8 1TL, UK*
[10] *Department of Astronomy, University of Virginia, 530 McCormick Road, Charlottesville, VA 22904-4325, USA*
[11]*Chalmers University of Technology, Department of Space, Earth and Environment, Onsala Space Observatory, 439 92 Onsala,Sweden*
[12]*Department of Physics, Toho University, 2-2-1 Miyama, Funabashi, Chiba 274-8510, Japan*
[13]*INAF - Osservatorio di Astrofisica e Scienza dello Spazio di Bologna, via Piero Gobetti 93/3, I-40129 Bologna, Italy*
[14]*National Radio Astronomy Observatory, 520 Edgemont Rd., Charlottesville VA 22903, USA*
[15]*Harvard-Smithsonian Center for Astrophysics, 60 Garden St., Cambridge, MA 02138, USA*
[16]*SRON Netherlands Institute for Space Research, Sorbonnelaan 2, 3584 CA Utrecht, The Netherlands*
[17]*Institute of Astronomy, The University of Tokyo, 2-21-1 Osawa, Mitaka, Tokyo 181-0015, Japan*
[18]*Research Center for the Early Universe, School of Science, The University of Tokyo, 7-3-1 Hongo, Bunkyo, Tokyo 113-0033, Japan*
[19]*Department of Astrophysical Sciences, Princeton University, Princeton, NJ 08544, USA*
[20]*National Astronomical Observatory of Japan, Osawa 2-21-1, Mitaka, Tokyo 181-8588, Japan*
[21]*Department of Physics, Nagoya University, Aichi 464-8602, Japan*
[22]*Institute for Advanced Research, Nagoya University Furocho, Chikusa-ku, Nagoya, 464-8602 Japan*
[23]*Department of Physics, University of Tokyo, Tokyo 113-0033, Japan*
[24]*Kavli Institute for the Physics and Mathematics of the Universe (Kavli IPMU, WPI), University of Tokyo, Chiba 277-8582, Japan*
[25]*Department of Physics, Nara Women's University, Kitauoyanishi-machi, Nara, Nara 630-8506, Japan*
[26]*Argelander-Institut für Astronomie, University of Bonn, Auf dem Hügel 71, 53121 Bonn, Germany*
[27]*AIM, CEA, CNRS, Université Paris-Saclay, Université Paris Diderot, Sorbonne Paris Cité, F-91191 Gif-sur-Yvette, France*
[28]*Department of Physics, McGill University, 3600 University Street Montreal, QC H3A 2T8, Canada*
[29]*Department of Physics, Faculty of Science, University of Zagreb, Bijenicka cesta 32, 10002 Zagreb, Croatia*
[30]*Graduate School of Natural Science & Technology, Kanazawa University, Kakuma-machi, Kanazawa, Ishikawa 920-1192, Japan*

MNRAS **000**, 1–32 (2019) Preprint 22 November 2019 Compiled using MNRAS LATEX style file v3.0

**ABSTRACT**

We present results from simultaneous modeling of high angular resolution GBT/MUSTANG-2 90 GHz Sunyaev-Zeldovich effect (SZE) measurements and XMM-XXL X-ray images of three rich galaxy clusters selected from the HSC-SSP Survey. The combination of high angular resolution SZE and X-ray imaging enables a spatially resolved multi-component analysis, which is crucial to understand complex distributions of cluster gas properties. The targeted clusters have similar optical richnesses and redshifts, but exhibit different dynamical states in their member galaxy distributions; a single-peaked cluster, a double-peaked cluster, and a cluster belonging to a supercluster. A large-scale residual pattern in both regular Compton-parameter $y$ and X-ray surface brightness distributions is found in the single-peaked cluster, indicating a sloshing mode. The double-peaked cluster shows an X-ray remnant cool core between two SZE peaks associated with galaxy concentrations. The temperatures of the two peaks reach $\sim 20-30$ keV in contrast to the cool core component of $\sim 2$ keV, indicating a violent merger. The highest SZE signal for the supercluster is elongated along a direction perpendicular to the major axis of the X-ray core, suggesting a minor merger before core passage. The $S_X$ and $y$ distributions are thus perturbed at some level, regardless of the optical properties. We find that an integrated Compton $y$ parameter and a temperature for the major merger are significantly boosted from those expected by the weak-lensing mass and those for the other two clusters show no significant deviations, which is consistent with predictions of numerical simulations.

**Key words:** galaxies: clusters: general - galaxies: clusters: intracluster medium- X-rays: galaxies: clusters - gravitational lensing: weak - radio continuum: galaxies

## 1 INTRODUCTION

Galaxy clusters, whose compositions are dominated by dark matter, ionised gas and galaxies, are the largest gravitationally bound objects in the Universe. The abundance of galaxy clusters is sensitive to the growth of matter density perturbations, and thus serves as a cosmological probe. Thanks to recent technical progress, galaxy clusters can be discovered by various observational methods; optical (e.g. Rykoff et al. 2014; Oguri 2014; Rozo et al. 2016; Oguri et al. 2018), X-ray (e.g. Böhringer et al. 2004; Piffaretti et al. 2011; Adami et al. 2018), thermal Sunyaev-Zel'dovich effect (SZE) (e.g. Planck Collaboration et al. 2014; Bleem et al. 2015; Sifón et al. 2016) and weak-lensing mass reconstruction (e.g. Miyazaki et al. 2007, 2018b). Optical techniques are unbiased against cluster mergers which non-linearly change properties of the the intracluster medium (ICM), but suffer from projection effects along the line of sight (Okabe et al. 2019). As X-ray emission from the ICM is proportional to the square of the electron number density, projection effects are less important but this technique suffers from a cool core bias (Eckert et al. 2011; Rossetti et al. 2017). The surface brightness of the thermal SZE is proportional to the line of sight integral of the ICM electron pressure, and is independent of redshift (see e.g. Birkinshaw 1999; Mroczkowski et al. 2019). Shear-selected clusters by the weak-lensing technique (Miyazaki et al. 2018b) do not rely on any baryonic physics but potentially suffer from projection bias in lensing signals. Since the redshift dependence, the tracer used (ICM, galaxies or mass), and the biases of each method are all different, all these techniques are complementary to each other. It is therefore important for the upcoming era of cluster cosmological studies to understand the selection function that arises in the construction of cluster catalogues from the true cluster population. In particular, it is essential to understand the baryonic physics as a function of dynamical state and the interplay between dark matter and baryons.

The Hyper Suprime-Cam Subaru Strategic Program (HSC-SSP; Aihara et al. 2018b,a; Miyazaki et al. 2018a; Komiyama et al. 2018; Kawanomoto et al. 2018; Furusawa et al. 2018; Bosch et al. 2018; Huang et al. 2018; Coupon et al. 2018; Aihara et al. 2019) is an on-going wide-field optical imaging survey composed of three layers of different depths (Wide, Deep and UltraDeep). The Wide layer is designed to obtain five-band (*grizy*) imaging over 1400 deg$^2$. The HSC-SSP Survey has both excellent imaging quality ($\sim$0.7 arcsec seeing in $i$-band) and deep observations ($r \lesssim 26$ AB mag). Therefore, the HSC survey currently has the best performance to search simultaneously for galaxy clusters and to measure their weak-lensing masses (for review; Pratt et al. 2019). Oguri et al. (2018) constructed a cluster catalogue using the *Cluster finding Algorithm based on Multi-band Identification of Red-sequence gAlaxies* (CAMIRA; Oguri 2014), which is a red-sequence cluster finder that exploits stellar population synthesis model fitting. The catalogue contains $\sim 1900$ clusters at $0.1 < z < 1.1$ with richness larger than $N = 15$ in the $\sim 240$ deg$^2$ HSC-SSP S16A field. The accuracy of photometric redshifts of the clusters is $\sigma_z/(1+z) \sim 0.01$ for the whole redshift range. Compared to shallower data from the Sloan Digital Sky Survey (SDSS; Rykoff et al. 2014; Oguri 2014) and the Dark Energy Survey (DES; Rykoff et al. 2016), many

⋆ Based on data collected at Subaru Telescope, which is operated by the National Astronomical Observatory of Japan. Based on observations obtained with XMM-Newton, an ESA science mission with instruments and contributions directly funded by ESA Member States and NASA

† E-mail:okabe@hiroshima-u.ac.jp

clusters beyond $z \sim 0.8$ were discovered (Oguri et al. 2018). Okabe et al. (2019) found $\sim$ 190 major-merger candidates using a peak-finding method of galaxy maps of the CAMIRA clusters and confirmed that the mass ratio of the sub and main halo is higher than 0.1 based on stacked weak-lensing analysis. Our statistical approach uncovers merger boosts in stacked *ROSAT* $L_X$ and *Planck* SZE scaling relations for the CAMIRA clusters and equatorial-shock-heated gas in cluster outskirts (Ricker & Sarazin 2001; ZuHone 2011; Ha et al. 2018) in both stacked X-ray and SZE images. However, using a stacked analysis makes it difficult to discriminate between the dynamical states of individual clusters, such as pre- and post- mergers. In principal, the optical CAMIRA clusters contain various dynamical states and stages (relaxed, minor merger, major merger, pre-merger, and post-merger), and thus systematic multi-wavelength follow-up studies of individual clusters are critically important to understand the relationship between gas properties and dynamical states in more details.

In this paper, we carry out joint SZE and X-ray studies of three CAMIRA clusters exhibiting different dynamical states to derive gas distributions, and compare the gas properties with optical properties and weak-lensing masses. The SZE data were taken using MUSTANG-2 (Dicker et al. 2014; Romero et al. 2019) installed on the 100-meter Green Bank Telescope (GBT). MUSTANG-2 has an angular resolution of 9 arcsec full-width half-maximum (FWHM) at 90 GHz and an instantaneous field of view of 4.25 arcmin, well matched to our resolution requirement and the angular size of our clusters. We use X-ray images from the XXL Survey (Pierre et al. 2016; Pacaud et al. 2016; Giles et al. 2016; Lieu et al. 2016; Pompei et al. 2016; Adami et al. 2018; Guglielmo et al. 2018) that is the largest observing program undertaken by *XMM-Newton*. The XXL Survey covers two distinct sky areas for a total of 50 square degrees down to a sensitivity of $6 \times 10^{-15}\,\mathrm{erg\,cm^{-2}\,s^{-1}}$ for point-like sources ([0.5-2] keV band). The XXL survey provides us with the unique, complementary X-ray data set for the joint analysis. We use the HSC-SSP Survey data for optical and weak-lensing analyses.

This paper is organized as follows. Sec. 2 describes our target properties. Sec. 3 presents our observations, a method of joint SZE and X-ray analysis, and our weak-lensing analysis. Sec. 4 is devoted to the results and discussion, respectively. We summarize our results in Sec. 5. Throughout this paper we use $\Omega_{m,0} = 0.3$, $\Omega_{\Lambda,0} = 0.7$ and $H_0 = 70h_{70}\,\mathrm{km\,s^{-1}\,Mpc^{-1}}$.

## 2 TARGETS

We selected three clusters (Table 1) at redshifts of $z \sim 0.4$ from the sample of the HSC-SSP CAMIRA clusters (Oguri et al. 2018) to observe with MUSTANG-2. As described in Sec 3.1, recovery of faint signals on angular scales larger than an instrument's instantaneous field-of-view (FOV), can be problematic. Clusters with angular sizes comparable to MUSTANG-2's $\approx$ 4.25 arcmin FOV are at medium ($z \sim 0.4$) to high ($z > 1.0$) redshifts, making them well-suited for MUSTANG-2 follow-up. However X-ray observations suffer from strong cosmological dimming and so for joint MUSTANG-2/X-ray analysis, the choice of $z \approx 0.4$ is close to optimal. At these redshifts, the 9 arcsec FWHM resolution of MUSTANG-2 enables us to resolve the pressure distribution with physical resolution of $\sim$ 60 kpc. The point spread function (PSF) of *XMM-Newton* is comparable to the angular resolution of MUSTANG-2, and a joint analysis of MUSTANG-2 SZE and XXL X-ray observation enables measurements of the two dimensional distributions of electron number density, temperature, pressure, and entropy parameter, all with reasonably high angular resolution.

As pointed out by Okabe et al. (2019), optically-selected clusters are free from bias against the ICM merger boost because the number of luminous red galaxies is essentially conserved during cluster mergers, but X-ray and SZE observables are affected by cluster merger phenomena. This is simply caused by the collisionless nature of member galaxies and collisional particles of the ICM. Thus, the sample of optical clusters, composed of a wide range of various dynamical states, is a very well-suited sample to investigate dynamical dependence of gas properties.

As our first observation, we selected three representative clusters of different galaxy distributions (Table 1) from the CAMIRA catalogue (Oguri et al. 2018) based on galaxy distributions (Okabe et al. 2019). We first constructed Gaussian smoothed maps (FWHM = $200h_{70}^{-1}$ kpc) of number densities of red galaxies selected in the colour-magnitude plane. We then identified peaks above a redshift-dependent threshold considering the contamination of extended galaxy distributions from nearby peaks caused by the smoothing procedure. The threshold was empirically determined to be an average peak stacked over the CAMIRA clusters at each redshift slice. The multi-peaked clusters are likely to be major-merger candidates by stacked weak-lensing analysis. The method cannot resolve substructures within the smoothing scale, less massive subhalos. We cannot discriminate between pre- and post- mergers due to the collisionless feature of galaxies.

The first cluster, HSC J022146-034619, is classified as single-peaked in galaxy distribution within the projected radius of 2 Mpc. As shown in the top-right panel of Figure 1, the galaxy distribution is concentrated around the cluster center. The second cluster, HSC J023336-053022, exhibits two galaxy peaks separated by about 520 kpc (the middle-right panel of Figure 1). The third cluster, HSC J021056-061154, shows an irregular galaxy distribution (the bottom-right panel of Figure 1). At a 200 kpc smoothing scale, the galaxy distribution has a single peak. This cluster is a part of the supercluster at $z = 0.43$ discovered by Pompei et al. (2016). As a mass proxy, we adopt cluster richness, $N \gtrsim 40$, as a selection function, which corresponds to $M_{500} \gtrsim 2 \times 10^{14} h_{70}^{-1} M_\odot$ (Okabe et al. 2019).

## 3 OBSERVATION AND DATA ANALYSIS

### 3.1 GBT/MUSTANG-2 SZE analysis

MUSTANG-2 (Dicker et al. 2014) is a 223-feedhorn bolometer camera installed on the 100 m GBT[1]. It has an angular resolution of 9 arcsec full-width half-maximum (FWHM)

[1] The Green Bank Observatory is a major facility supported by the National Science Foundation and operated under cooperative agreement by Associated Universities, Inc.

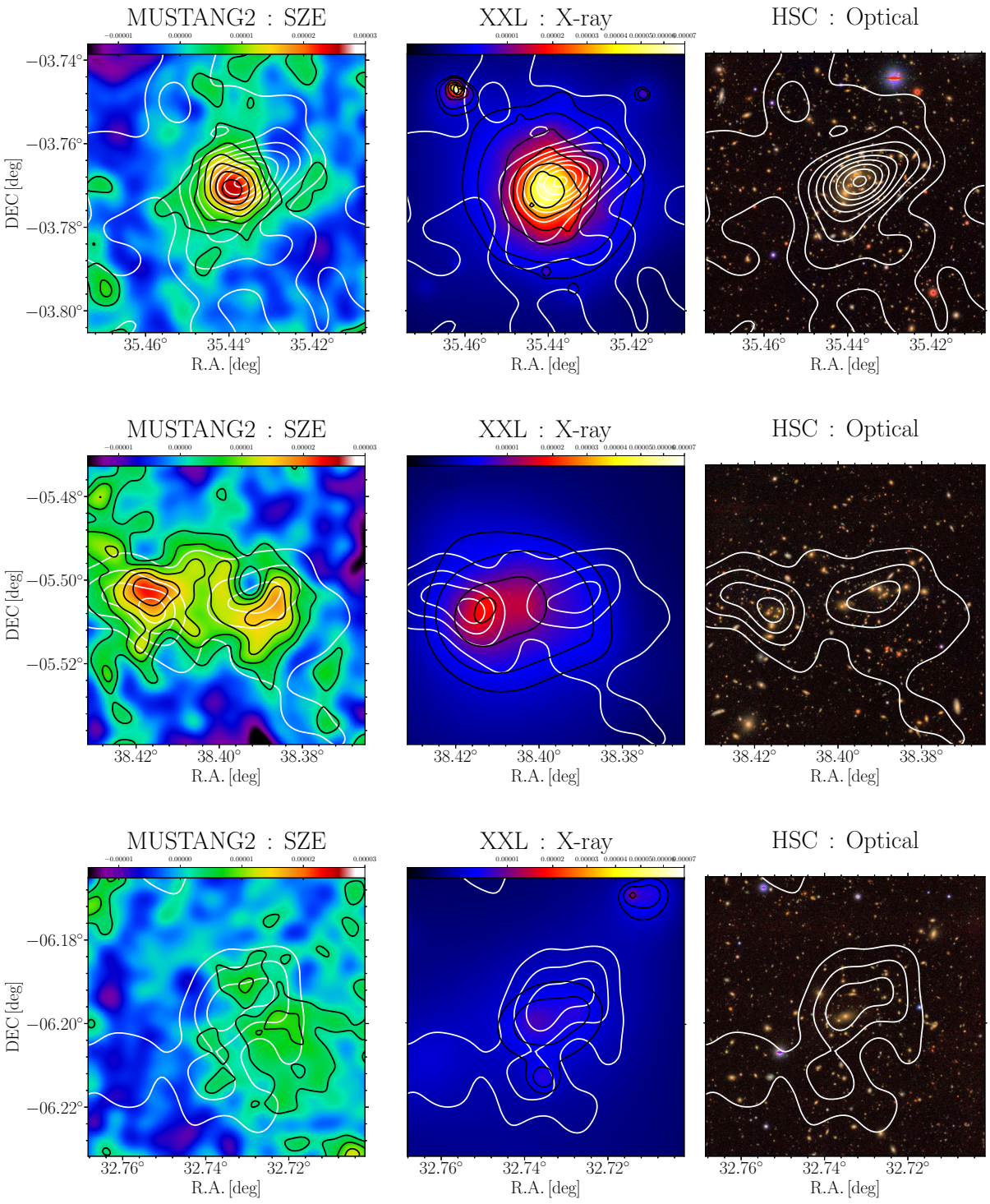


**Figure 1.** SZE (left), X-ray (middle) and optical (right) imaging (4 arcmin × 4 arcmin) for the three targeted clusters (from the top to the bottom; HSC J022146-034619, HSC J023336-053022, and HSC J021056-061154). *Left*: GBT/MUSTANG-2 Compton $y-$map with Gaussian smoothing ($\sigma$ = 8 arcsec) of raw images, yielding an effective resolution of 12.5 arcsec. The black contours are at $y = [3, 7, 11, 15, 19, 23] \times 10^{-6}$. The RMS noises within 1 arcmin from the center of FOV of the smoothed map are $y = 2, 6,$ and $3 \times 10^{-6}$ from the top to the bottom, respectively. The green and red colours show positive $y$ values and the blue and purple colours show negative values. Color scales are the same for all the clusters. White contours are galaxy distributions, taken from the right panel. *Middle*: adaptively smoothed X-ray images in the soft band ($0.5-2.0$ keV) from the XXL survey. Black contours denote X-ray surface brightness ($[4, 5.4, 9.8, 17, 27, 40] \times 10^{-6}$ ct s$^{-1}$). The white contours are the same as those in the right panel. Color scales are the same for all the clusters. *Right:* HSC-SSP optical *riz*-color image overlaid with galaxy contours (white) smoothed with a $\sigma = 200$ kpc Gaussian (Okabe et al. 2019). Each contour is stepped by two additional luminous member galaxies, starting at a level of two luminous galaxies.

**Table 1.** Properties of the clusters. [a)] cluster richness from the CAMIRA catalogue (Oguri et al. 2018). [b)] X-ray temperature within 300 kpc (Adami et al. 2018). [c)]: gas properties revealed by this paper. †: Okabe et al. (2019). ‡: Pompei et al. (2016).

| CAMIRA Name | Optical Morphology | RA [deg] | DEC [deg] | $z$ | $N^{a)}$ | XXL name | $k_B T^{b)}_{300\mathrm{kpc}}$ [keV] | Dynamical State[c)] |
|---|---|---|---|---|---|---|---|---|
| HSC J022146-034619 | single-peaked† | 35.441 | -3.772 | 0.433 | 69 | XLSSC 006 | $4.2 \pm 0.5$ | sloshing |
| HSC J023336-053022 | double-peaked† | 38.398 | -5.506 | 0.436 | 47 | XLSSC 105 | $6.0 \pm 1.0$ | post-major merger |
| HSC J021056-061154 | supercluster‡ | 32.735 | -6.198 | 0.429 | 41 | XLSSC 083 | $5.1 \pm 0.9$ | pre-minor merger |

and a 75–105 GHz bandpass. The instantaneous field of view is 4.25 arcmin. We observed each cluster with a 3 arcmin radius daisy scan pattern similar to that used for other clusters by MUSTANG-2 (Romero et al. 2019), spending 6.5, 10, and 4.6 hours on-source for HSC J022146-034619, HSC J023336-053022, and HSC J021056-061154, respectively. Every 20 minutes pointing and focus checks were carried out on 0217+0144 allowing us to calibrate out drifts in detector gains or the atmosphere. Several times a night this source was tied to observations of Uranus for absolute calibration. Stacked observations of the calibrators allowed recovery of the *effective* beamshape of the GBT. This beam includes any filtering in the mapmaker, near sidelobes from focus drifts, and any remaining pointing errors.

Data were reduced using the MIDAS data pipeline. Briefly, this pipeline first calibrates each detector with gains and beam volumes extrapolated between each observation of the point source 0217+0144. The astronomical signal is mostly between ∼0.1 Hz (i.e. ∼ 10 seconds, the time to scan across the map) and ∼10 Hz (i.e. ∼ 0.1 seconds, the time taken to scan across a point source). At lower frequencies the signal is dominated by $1/f$ noise from the atmosphere and at higher frequencies there is noise from electrical pickup. A Fourier filter (0.08–30 Hz bandpass) is applied to each detector timestream greatly improving data quality. After this, problematic detectors (for example ones with low gain or high noise) are flagged along with portions of data showing glitches. At this stage the timestreams are dominated by atmospheric emission. This can be removed using a principal component analysis to produce cleaned timestreams which are made into the maps presented in this paper. More details of the MIDAS pipeline can be found in Romero et al. (2019).

Although the MIDAS pipeline reduces the RMS in the raw timestreams by several orders of magnitude, the maps it produces are not unbiased. Structure on angular scales significantly larger than the size of the FOV are diminished in brightness. This can be characterized by an angular transfer function ($f_{\mathrm{TF}}$; $Figure 2$). When quantitatively comparing observational data to model fits, it is essential to correct for this transfer function (Sec 3.3). The transfer function is calculated by passing randomized sky structure with equal power on all spatial scales through simulated observing software which produces time ordered data for a set of scans identical to those for each cluster. Those time-streams are then processed with the same filtering as is done on the real data and maps of the given instance of randomized sky are output. The transfer function is defined as the ratio in Fourier space of the power spectrum of the reconstructed image to the power spectrum of the input map (Figure 2).

The rest of the analysis of the MUSTANG-2 data presented in this paper is carried out in map space. We follow Romero et al. (2015, 2017, 2019) for point source removal. To calculate cluster profiles we use radial averaging in segments (either 90 or 45 degrees) to bring down the noise/get higher accuracy in the profiles without compromising the ability to resolve the shape of the cluster.

As well as the transfer function, knowledge of the effective beam shape in the maps is critical. As described above, we made stacked beam maps for each cluster using 0217+0144. These beams were well described by the double Gaussian fit. A primary and secondary beam of an average of the three clusters have FWHM of 9.7 arcsec and 54 arcsec, respectively. The peak ratio of the secondary beam is $\sim 5 \times 10^{-3}$ of the primary one. The secondary beam agrees with the expected near-sidelobes on the GBT given the MUSTANG-2 illumination pattern and medium-scale aperture phase errors not fully corrected by the out-of-focus (OOF) procedure.

### 3.2 XXL X-ray analysis

We here briefly describe X-ray analysis of the XXL Survey (Pierre et al. 2016). We processed the XXL data using the XMMSAS package and calibration files v10.0.2 and the data reduction pipeline (Pacaud et al. 2016) in order to obtain cleaned event files for each observation. We extracted photon images in the [0.52.0] keV band for each EPIC instrument and created co-added EPIC images by summing the images obtained for each detector. In this paper, we use the co-added images in model fittings described in Sec. 3.3.

We compare our results with X-ray complementary quantities from the literature, and briefly describe measurement methods. The measurement of the electron number density profile is described in detail by Eckert et al. (2017). The electron number density is measured by a deprojection method using surface brightness profiles that were extracted for each cluster using Proffit (Eckert et al. 2011). The X-ray temperature is measured and described in detail by Giles et al. (2016). The X-ray spectra are extracted within a circular aperture of 300 kpc centered on the X-ray positions. The background is measured from an annulus centred on the cluster with the inner radius set to the detection radius and the outer radius as 400 arcsec. The resulting temperatures are summarized in Table 1. Since there is deep X-ray pointing data (Obs Id:0604280101) for HSC J022146-034619 (XLSSC006), we also measure X-ray temperature profile following the XMM-Newton cluster outskirts project (XCOP; Eckert et al. 2017; Ghirardini et al. 2018; Ettori et al. 2019; Eckert et al. 2019).

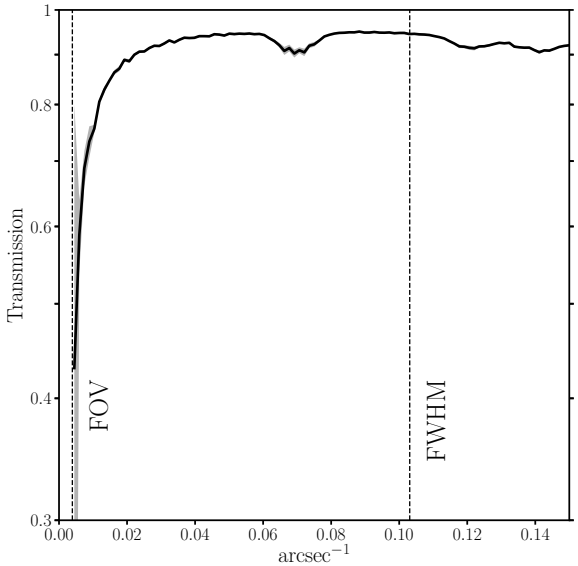


**Figure 2.** Effective average transfer function for our sample of clusters, $\hat{f}_{\rm TF}$, as a function of angular wavenumber $k$ [arcsec$^{-1}$]. The gray transparent region at low $k$ shows that at low $k$ a few points have large error bars. The transfer functions of individual clusters are calculated as the square root of the ratio of the one-dimensional power spectra of the observed fake sky and input fake sky. Vertical dashed lines denote the relevant angular wavenumbers for the FOV and FWHM.

### 3.3 Gas modeling

We employ a Bayesian forward modeling method to measure gas properties of the ICM. In the modeling, we introduce a generalized Navarro, Frenk, and White profile (hereafter, gNFW; Navarro et al. 1997; Nagai et al. 2007b; Mroczkowski et al. 2009; Arnaud et al. 2010; Planck Collaboration et al. 2011; Okabe et al. 2014a) of the electron number density and the temperature of the ICM,

$$n_e(r) = n_0 \left(\frac{r}{r_s}\right)^{-\gamma_n} \left(1+\left(\frac{r}{r_{s,n}}\right)^{\alpha_n}\right)^{-\beta_n}, \quad (1)$$

$$T_e(r) = T_0 \left(\frac{r}{r_s}\right)^{-\gamma_T} \left(1+\left(\frac{r}{r_{s,T}}\right)^{\alpha_T}\right)^{-\beta_T}. \quad (2)$$

Here, $r$ is three-dimensional radius from cluster center. We note that the notations of slope parameters are different from definitions of Nagai et al. (2007a) in order to clarify parameter degeneracy during the analysis. We assume a spherically symmetric model with $\alpha_n = \alpha_T = 2$. When the inner slope $\gamma$ is additionally assumed to be $\gamma = 0$, the model corresponds to a $\beta$ model (Cavaliere & Fusco-Femiano 1976) which is well-used in X-ray analysis. The temperature scale radius, $r_{s,T}$, cannot be constrained well by a sharp $y$ distribution at $\theta > 1$ arcmin because of the transfer function. We therefore adopt $r_{s,n} = r_{s,T} = r_s$. The electron pressure is directly calculated by $P_e = n_e k_B T_e$.

The SZE Compton-$y$ parameter and X-ray surface brightness are expressed as a geometrical projection of the spherical profiles along the line of sight,

$$y(R) = \frac{\sigma_T}{m_e c^2} \int P_e(R,l) dl, \quad (3)$$

$$S_X(R) = S_0 \int n_e(R,l)^2 dl + S_b \quad (4)$$

where $r^2 = R^2 + l^2$, $R$ is the projected radius from the cluster center, and $l$ is the distance along the line of sight. Here, $\sigma_T$ is the Thomson cross-section for electron scattering, $m_e$ is the electron mass and $c$ is the light velocity. Since the X-ray soft-band emissivity ($0.5-2.0$ keV) is almost independent of gas temperature (Ettori et al. 2013), we ignore the temperature dependence. $S_b$ and $S_0$ are the background components for X-ray data and the conversion factor from the electron number density to the X-ray surface brightness, respectively.

Given the model, we compute actual SZE and X-ray measurements on the sky taking into account the instrument spatial responses, namely, the point spread function (PSF) and the radial transfer function of the MUSTANG-2 (Sec 3.1). We pixelize the models onto a regular grid of angular position $\boldsymbol{\theta}$ ($\theta = R/D_A$) and then convolve them with the instrument response function using the two-dimensional Fourier transform ($\mathcal{F}T$),

$$\tilde{y}_m(\boldsymbol{\theta}) = (f_{\rm PSF}^{\rm SZ} f_{\rm TF}) \otimes y(\boldsymbol{\theta}) \quad (5)$$

$$\tilde{S}_{X,m}(\boldsymbol{\theta}) = f_{\rm PSF}^{\rm X} \otimes S_X(\boldsymbol{\theta}) \quad (6)$$

where $f_{\rm TF}$ ($\hat{f}_{\rm TF} = \mathcal{F}T(f_{\rm TF})$) and $f_{\rm PSF}^{\rm SZ}$ are the transfer function and the PSF of the GBT/MUSTANG-2, respectively, and $f_{\rm PSF}^{\rm X}$ is the PSF of the *XMM-Newton*. We use the transfer functions and PSFs of individual clusters.

Since the X-ray surface brightness depends on only the electron number density and the $y$ parameter is specified by both the electron number density and temperature, the constraints imposed by the SZE and X-ray data enables us to resolve a degeneracy between the number density and temperature in the $y$ parameter and then model the three-dimensional profiles under the assumption of spherically symmetric distributions. We therefore simultaneously fit the SZE and X-ray data with the models (eqs. 5-6), in a similar manner to X-COP (Eckert et al. 2017; Ghirardini et al. 2018; Ettori et al. 2019; Eckert et al. 2019) and other studies (e.g. Ruppin et al. 2019). The joint log-likelihood is written as

$$-2\ln\mathcal{L} = \sum_i \frac{(\tilde{y}_{d,i} - \tilde{y}_{m,i})^2}{\sigma_{y,i}^2} + \sum_j \frac{(\tilde{S}_{Xd,j} - \tilde{S}_{Xm,j})^2}{\sigma_{X,j}^2} + {\rm const}, \quad (7)$$

where $\tilde{y}_d$ and $\sigma_y$ are the MUSTANG-2 measurements of $y$ parameter and statistical errors and $\tilde{S}_{Xd}$ and $\sigma_X$ are the X-ray surface brightness distribution and statistical errors, respectively. We do not include the X-ray temperature measurement in the joint likelihood, because the spatial resolution of the spectroscopic measurement is much worse than those of $y$ and $S_X$ distributions. Since $n_0$, $T_0$ and $r_s$ are positive parameters, we treat them as logarithmic quantities in our fitting procedures. All quantities are estimated using a central biweight in order to down-weight outliers in skewed posterior distributions.

In the Bayesian modeling, we use radial profiles computed with logarithmic binning and linearly pixelised maps as the data array of $y$ and $S_X$ of eq. 7. The former and

latter methods are called one- and two- dimensional analyses, respectively. The former method is effective at reducing computational time and good at constraining the inner slopes of the electron number density and temperature profiles. We convert from the PSF-convolved maps to radial profiles in computing the likelihood. We choose XXL centers as central positions except for the major-merger case. The latter method is time-consuming but can consider multiple components of the ICM and treat cluster centers as free parameters. We use $S_X$ and $y$ maps binned with pixel size of 10 or 20 arcsec to reduce computational time, and thus the angular resolution of the central distributions is worse than that in the one-dimensional analysis. Therefore, the two analyses are complementary to each other. We exclude regions around $\sim 0.3$ arcmin in radius centering radio point or X-ray point sources in computing the log-likelihood.

### 3.4 Weak-lensing Mass Measurement

We describe weak-lensing (WL) analyses of individual clusters. Since the signal-to-noise ratio of the WL data is much lower than those of the X-ray and SZE imaging, we do not include a weak-lensing likelihood in the joint likelihood (eq. 7) but independently measure individual cluster masses. The independent analysis has the advantage that it does not impose the assumption of hydrostatic equilibrium (HE) in the modeling (e.g. Okabe & Umetsu 2008).

For a shape measurement, we use the re-Gaussianization method (Hirata & Seljak 2003) which is implemented in the HSC pipeline (see details in Mandelbaum et al. 2018a). Only galaxies satisfying the full-color and full-depth criteria from the HSC galaxy catalogue were used in both our precise shape measurements and photometric redshift estimations. We select background galaxies behind each cluster using the color-color selection following Medezinski et al. (2018a).

The dimensional, reduced tangential shear $\Delta\Sigma_+$ in the $k-$th radial bin can be computed by azimuthally averaging the measured tangential ellipticity, $e_+ = -(e_1 \cos 2\varphi + e_2 \sin 2\varphi)$;

$$\Delta\Sigma_+(R_k) = \frac{\sum_i e_{+,i} w_i \langle \Sigma_{\rm cr}(z_l, z_{s,i})^{-1} \rangle^{-1}}{2\mathcal{R}(R_k)(1+K(R_k))\sum_i w_i}, \tag{8}$$

(e.g. Miyaoka et al. 2018; Medezinski et al. 2018b; Okabe et al. 2019; Miyatake et al. 2019; Murata et al. 2019). The inverse of the mean critical surface mass density for the $i$-th galaxy is computed by the probability function $P(z)$ from the machine learning method (MLZ; Carrasco Kind & Brunner 2014) calibrated with spectroscopic data (Tanaka et al. 2018),

$$\langle \Sigma_{\rm cr}(z_l, z_s)^{-1} \rangle = \frac{\int_{z_l}^{\infty} \Sigma_{\rm cr}^{-1}(z_l, z_s) P(z_s) dz_s}{\int_0^{\infty} P(z_s) dz_s}, \tag{9}$$

where $z_l$ and $z_s$ are the cluster and source redshift, respectively. The critical surface mass density is expressed as $\Sigma_{\rm cr} = c^2 D_s / 4\pi G D_l D_{ls}$, where $D_l$, $D_s$ and $D_{ls}$ are the angular diameter distances from the observer to the cluster, to the sources and from the lens to the sources, respectively. The radius positions, $R_k$, is defined by the weighted harmonic mean (Okabe & Smith 2016). We adopt the same central position as that of one-dimensional SZE and X-ray analysis. The dimensional weighting function is given by

$$w = \frac{1}{e_{\rm rms}^2 + \sigma_e^2} \langle \Sigma_{\rm cr}^{-1} \rangle^2 \tag{10}$$

where $e_{\rm rms}$ and $\sigma_e$ are the root mean square of intrinsic ellipticity and the measurement error per component ($\alpha = 1$ or 2), respectively. The shear responsivity, $\mathcal{R}$, and the calibration factor, $K$, are obtained by $\mathcal{R} = 1 - \sum_{ij} w_{i,j} e_{{\rm rms},i}^2 / \sum_{ij} w_{i,j}$ and $K = \sum_{ij} m_i w_{i,j} / \sum_{ij} w_{i,j}$ with the multiplicative shear calibration factor $m$ (Mandelbaum et al. 2018a,b), respectively. We also conservatively subtract an additional, negligible offset term for calibration.

We use the NFW profile (Navarro et al. 1996) for individual cluster mass measurements. The generalized version of the NFW model (gNFW; eqs 1-2) is too complicated for low signal-to-noise ratio lensing profiles of individual clusters, and thus its slope parameters cannot be constrained. The gNFW model can be constrained by the stacked lensing profile measured with high signal-to-noise ratio (e.g. Okabe et al. 2013; Okabe & Smith 2016; Umetsu et al. 2016). The three-dimensional mass density profile of the NFW profile is expressed as,

$$\rho_{\rm NFW}(r) = \frac{\rho_s}{(r/r_s)(1+r/r_s)^2}, \tag{11}$$

where $r_s$ is the scale radius and $\rho_s$ is the central density parameter. The NFW model is also specified by the spherical mass, $M_\Delta = 4\pi\Delta\rho_{\rm cr} r_\Delta^3/3$, and the halo concentration, $c_\Delta = r_\Delta / r_s$. Here, $r_\Delta$ is the overdensity radius. We treat $M_\Delta$ and $c_\Delta$ as free parameters. By integrating the mass density profile along the line of sight, we compute the model of the reduced tangential shear, $f_{\rm model}$, defined by

$$f_{\rm model}(R) = \frac{\bar{\Sigma}(<R) - \Sigma(R)}{1 - \mathcal{L}_z \Sigma(R)}, \tag{12}$$

where $\Sigma(R)$ is the local surface mass density at the projected radius $R$, $\bar{\Sigma}(<R)$ is the average surface mass density within the projected radius $R$, and $\mathcal{L}_z = \sum_i \langle \Sigma_{{\rm cr},i}^{-1} \rangle w_i / \sum_i w_i$. Given the mass model, the log-likelihood of the weak-lensing analysis is described by

$$-2\ln\mathcal{L}_{\rm WL} = \ln(\det(C_{km})) + \sum_{k,m} (\Delta\Sigma_{+,k} - f_{\rm model}(R_k)) C_{km}^{-1} (\Delta\Sigma_{+,m} - f_{\rm model}(R_m)), \tag{13}$$

where $k$ and $m$ denote the $k-$th and $m-$th radial bins. The covariance matrix, $C$, is composed of the uncorrelated large-scale structure (LSS), $C_{\rm LSS}$, along the line of sight (Schneider et al. 1998), the shape noise $C_g$ and the errors of the source redshifts, $C_s$ (e.g. Pratt et al. 2019). The elements of LSS lensing covariance matrix are correlated with each other.

We also carry out the NFW model fitting with a free central position using two-dimensional shear pattern (Oguri et al. 2010). The log-likelihood is defined as

$$-2\ln\mathcal{L}_{\rm WL} = \sum_{\alpha,\beta=1}^{2} \sum_{k,m} \left[\Delta\Sigma_{\alpha,k} - f_{{\rm model},\alpha}(\boldsymbol{R}_k)\right] \boldsymbol{C}_{\alpha\beta,km}^{-1} \times \left[\Delta\Sigma_{\beta,m} - f_{{\rm model},\beta}(\boldsymbol{R}_m)\right] + \ln(\det(C_{\alpha\beta,km})). \tag{14}$$

Here, the subscripts $\alpha$ and $\beta$ denote each shear component. The central positions are restricted to full-width boxes 2 arcmin $\times$ 2 arcmin centered on the brightest cluster galaxies

(BCGs). The two-dimensional analysis is good at determining the central positions (Oguri et al. 2010) and measuring masses of multi-components of merging clusters (Okabe et al. 2011, 2015; Medezinski et al. 2016).

In actual analyses, the maximum radial range to compute $\Delta\Sigma_\alpha$ is determined by excluding neighboring, massive CAMIRA clusters to avoid their contamination in lensing signals. We adopt an adaptive radial-bin choice (Okabe et al. 2016) for cluster mass estimation. The shape catalogue in the central region of HSC J021056-061154 is not provided because the region does not satisfy the full-colour and full-depth condition of the shape measurement. We thus measure WL masses without the central region of HSC J021056-061154.

## 4 RESULTS AND DISCUSSION

### 4.1 HSC J022146-034619

#### *4.1.1 Joint analysis*

As shown in the top panel of Figure 1, the two-dimensional distributions of the member galaxies, $y$-parameter and X-ray surface brightness have a single peak around the BCG, coinciding within the PSF or smoothing scale of the observation. The $y$ and $S_X$ distributions exhibit regular morphology, while the red member galaxy distribution is elongated to the northwest direction.

We measure the $y$ and $S_X$ radial profiles, and fit them with the gNFW model (eqs.1-2) using uniform priors. In order to discriminate between the actual observations and the non-convolved models, we represent the observations by $\tilde{y}_d$ and $\tilde{S}_{Xd}$ (eq. 7). The best-fit parameters are summarized in Table 2. The best-fit $y$ and $S_X$ profiles are shown by the blue solid line in the top-left and top-middle panels of Figure 3. Due to the transfer function (see Figure 2) of the MUSTANG2 observation, the observed and best-fit $y$ profiles sharply decrease at $\theta > 1$ arcmin. In a very central region of $\theta \lesssim 0.07$ arcmin ($R \lesssim 20$ kpc) comparable to BCG scale, we find a significant discrepancy between the observed $\tilde{y}_d$ profile and the best-fit $\tilde{y}$ profile. Although we dropped the assumptions of $\alpha$ and $r_T$ in the gNFW profiles, the excess of the $y$-parameter cannot be explained by the gNFW model alone. In order to solve the discrepancy, we add the power-law model for the temperature profile (eq. 15) to the gNFW temperature model (eq. 2); $T_e = T_{\rm gNFW} + T_{\rm pow}$. The power-law model is specified by

$$T_e = T_{p0}\left(\frac{r}{r_0}\right)^{-p} \quad (15)$$

where $T_{p0}$ is the normalization, $r_0 = 1$ kpc is a pivot radius and $p$ is a slope. We refer to it as a gNFW+$T_{\rm pow}$ model. The best-fit parameters are summarized in the middle panel of Table 2 and shown by the green dashed lines in Figure 2. The best-fit profiles for the gNFW and gNFW+$T_{\rm pow}$ models are in good agreements at $\theta > 0.07$ arcmin.

The bottom panels of Figure 3 are, from left to right, the three-dimensional profiles of the pressure, the electron number density and the electron temperature. The errors shown by blue and green transparent regions are calculated by the error covariance matrix. The electron pressure profiles for the gNFW model and the gNFW+$T_{\rm pow}$ model have a flat core and a cuspy structure, respectively. The electron number density profiles for the two models are similar to each other. We compare with the deprojected electron number density and find a good agreement. The electron temperature profile for the gNFW model has a flat core, while the gNFW+$T_{\rm pow}$ model has a steep profile. The two profiles at $r > 200$ kpc agree well with each other.

We also measured X-ray temperature using deep X-ray data based on the X-COP method (Eckert et al. 2017). In X-ray temperature measurements of the 1st and 2nd inner bins, we consider a mixture of incoming photons at each annulus using Cross-arf in Xspec. The X-ray temperature profile agrees well with the SZE temperature profiles. However, the emission-weighted temperature using the XXL temperature ($4.2^{+0.5}_{-0.7}$ keV; Table 1) within 300 kpc is slightly lower than the X-COP measurement using deep X-ray data, but the discrepancy is only $2.3\sigma$ level.

We measure weak-lensing masses using a tangential shear profile (the left panel of Figure 4 and Table 3). A comparison of weak-lensing and HE masses is discussed in Sec 4.8.

#### *4.1.2 Sloshing Feature*

Both the $S_X$ and $y$ distributions for HSC J022146-034619 exhibit regular morphology in the sky plane in contrast to the other two clusters. However, in the gNFW profile alone it is difficult to explain the excess in the observed $\tilde{y}_d$ profile at very central region of $\theta \lesssim 4$ arcsec, corresponding to $R \lesssim 20$ kpc, as shown in Figure 3. The radial size is comparable to the beam radius. The excess requires the additional hot component. Since the three-dimensional profiles computed with and without the hot component agree well with each other on large scale, the global gas structure does not change and only local modification occurs. We also assume an elliptical gNFW temperature model elongated along the line of sight for fitting, but found it difficult to explain the excess by the reasonable parameter choices. Therefore, the feature implies that the gas is locally interacting, heated or perturbed.

A clearer display of this feature is shown in Figure 5, where we compute fractional residual $S_X$ and $y$ maps between the observed images and average images. The residual images ( $\delta\tilde{S}_X$ and $\delta\tilde{y}$ ) are derived by subtracting the averaged images. The average images are computed by azimuthally-averaged profiles through interpolation and thus free from any assumptions of analytical models. We then normalize them by the averaged images and obtain $\delta\tilde{S}_X/\langle\tilde{S}_X\rangle$ and $\delta\tilde{y}/\langle\tilde{y}\rangle$ to consider the radial dependence of $\langle\tilde{S}_X\rangle$ and $\langle\tilde{y}\rangle$. For *XMM-Newton*, there is a large CCD gap in the PN detector around the central region, and the residual map is computed from the MOS1 and MOS2 detectors. Since there are small CCD gaps even in MOS1 and MOS2, we independently compute $\delta\tilde{S}_X/\langle\tilde{S}_X\rangle$ excluding CCD gaps and then combined the two residual maps. For MUSTANG-2, the $\tilde{y}$ profile is negative at $\theta \gtrsim 1$ arcmin, and we thus mask the region to $\theta > 0.8$ arcmin. Since the XMM pixel size (2.5 arccec) is different from the MUSTANG-2 pixel size (1 arcsec), we computed the residual $y$ map using the XMM pixel size. Since the two residual maps are still noisy, we adopt Gaussian smoothing with $\sigma = 8$ arcsec which is the same as Figure 1. To avoid the masked region in the resid-

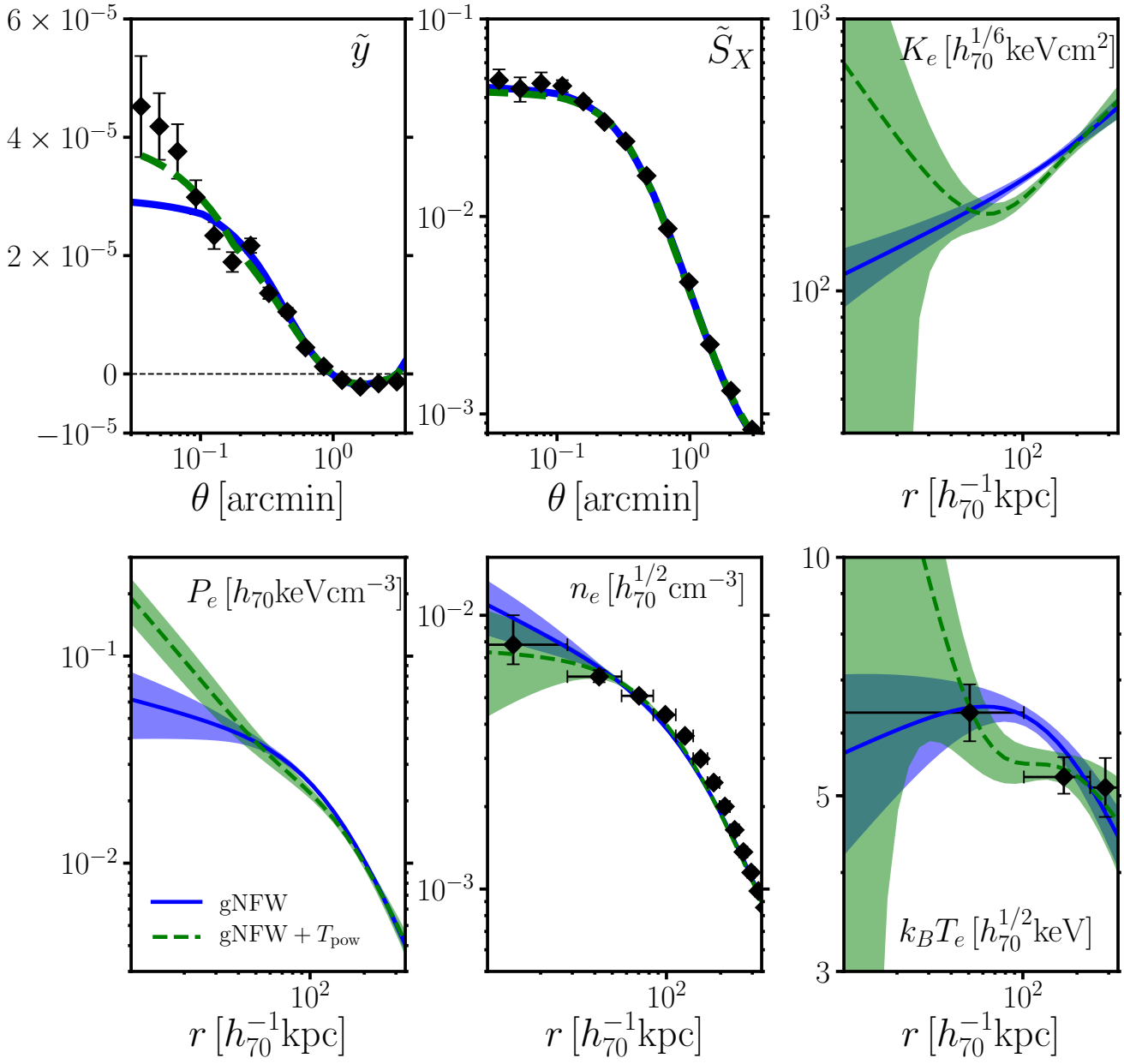


**Figure 3.** *Top*: $\tilde{y}$ (left) and $\tilde{S}_X$ (middle) profiles of HSC J022146-034619. The signal-to-noise ratios computed by the observed $\tilde{y}_d$ and $\tilde{S}_{Xd}$ profiles are $\sim 36\sigma$ and $\sim 100\sigma$, respectively. They are defined as $(\sum_{\tilde{y}_{d,i}>0} \tilde{y}_{d,i}^2/\sigma_{y,i}^2)^{1/2}$ and $(\sum_i (\tilde{S}_{X,i}-\tilde{S}_b)^2/\sigma_{X,i}^2)^{1/2}$, respectively. The blue solid and green dashed lines are the best-fit gNFW and gNFW+$T_{\mathrm{pow}}$ models derived from the joint SZE and X-ray analysis, respectively. The right panel shows the entropy index profile ($K_e$) computed from the bottom panels. The blue and green transparent regions are their $1\sigma$ errors. *Bottom*: Three-dimensional profiles of the best-fit pressure ($P_e$, left), density ($n_e$, middle) and temperature ($k_BT_e$, right). The black diamonds in the middle panel denote the model-independent, deprojected profile of the electron number density. The black diamonds in the right panel are X-ray temperature measured by deep X-ray data.

ual $y$ map, we conservatively limit the region at $\theta < 0.5$ arcmin at which $\tilde{y}$ is almost constant (Figure 3). The resulting residual maps are shown in Figure 5. Positive and negative excesses appear in the northern and southern areas in the two maps. The residual patterns are coherently distributed, which indicates a presence of gas sloshing. The gas disturbances could also triggers local heating (e.g. Ascasibar & Markevitch 2006; ZuHone et al. 2010; Vazza et al. 2012).

It is difficult to search by photometric information for a subhalo which triggered the sloshing mode. A large number of spectroscopic redshifts will be crucial to identity the subhalo, but only nine redshifts are available to date. Since the

**Table 2.** Best-fit gas model parameters. The upper and lower panels are the best-fits by the one-dimensional analysis and the multi-component two-dimensional analysis. The middle panel is the best-fits including the power-law model (pow) of the temperature for HSC J022146.

| Name | $n_0$ $[h_{70}^{1/2}\mathrm{cm}^{-3}]$ | $k_BT_0$ $[h_{70}^{1/2}\mathrm{keV}]$ | $r_s^{\rm gas}$ $[h_{70}^{-1}\mathrm{kpc}]$ | $\beta_n$ | $\gamma_n$ | $\beta_T$ | $\gamma_T$ |
|---|---|---|---|---|---|---|---|
| HSC J022146 | $4.66^{+1.30}_{-0.70}\times10^{-3}$ | $7.47^{+0.72}_{-0.48}$ | $137.48^{+22.46}_{-28.84}$ | $0.684^{+0.058}_{-0.033}$ | $0.328^{+0.076}_{-0.162}$ | $0.315^{+0.115}_{-0.043}$ | $-0.106^{+0.101}_{-0.151}$ |
| HSC J023336 | $1.34^{+0.43}_{-0.24}\times10^{-3}$ | $7.00^{+1.31}_{-0.86}$ | $523.64^{+100.39}_{-187.37}$ | $1.308^{+0.272}_{-0.274}$ | $0.428^{+0.067}_{-0.134}$ | $0.622^{+0.389}_{-0.232}$ | $-0.186^{+0.109}_{-0.170}$ |
| HSC J021056 | $5.39^{+6.35}_{-1.98}\times10^{-4}$ | $15.41^{+9.22}_{-5.59}$ | $525.30^{+629.61}_{-276.15}$ | $0.511^{+0.581}_{-0.158}$ | $0.579^{+0.052}_{-0.148}$ | $0.727^{+0.296}_{-0.246}$ | $-0.692^{+0.243}_{-0.685}$ |
| HSC J022146 (gNFW) | $6.96^{+4.33}_{-1.74}\times10^{-3}$ | $6.96^{+1.01}_{-1.04}$ | $99.03^{+30.00}_{-26.67}$ | $0.795^{+0.304}_{-0.092}$ | $0.263^{+0.228}_{-0.675}$ | $1.382^{+0.648}_{-0.733}$ | $-2.359^{+1.386}_{-1.090}$ |
| HSC J022146 (pow) | - | $0.86^{+1.20}_{-0.50}$ | - | - | - | - | $0.973^{+0.521}_{-0.287}$ |
| HSC J023336 (center) | $9.66^{+5.01}_{-2.82}\times10^{-4}$ | $11.64^{+2.14}_{-2.44}$ | $522.28^{+182.34}_{-130.00}$ | $1.229^{+0.285}_{-0.316}$ | $0.622^{+0.114}_{-0.190}$ | $0.914^{+0.345}_{-0.344}$ | $-1.370^{+0.720}_{-0.888}$ |
| HSC J023336 (east) | $5.49^{+1.12}_{-0.95}\times10^{-4}$ | $33.91^{+3.82}_{-6.54}$ | $322.40^{+28.87}_{-47.54}$ | 1 (fixed) | 0 (fixed) | 1 (fixed) | 0 (fixed) |
| HSC J023336 (west) | $3.77^{+1.72}_{-0.82}\times10^{-4}$ | $54.91^{+14.75}_{-14.57}$ | 322.40 (linked) | 1 (fixed) | 0 (fixed) | 1 (fixed) | 0 (fixed) |
| HSC J021056 (east) | $5.87^{+3.38}_{-2.20}\times10^{-4}$ | $16.37^{+10.03}_{-12.03}$ | $485.27^{+203.28}_{-169.00}$ | $0.920^{+0.514}_{-0.413}$ | $0.566^{+0.334}_{-0.288}$ | $1.458^{+0.353}_{-0.419}$ | $-1.128^{+0.556}_{-0.739}$ |
| HSC J021056 (west) | $5.10^{+0.58}_{-1.16}\times10^{-4}$ | $14.62^{+0.50}_{-1.43}$ | $551.15^{+46.30}_{-70.26}$ | 1 (fixed) | 0 (fixed) | 1 (fixed) | 0 (fixed) |

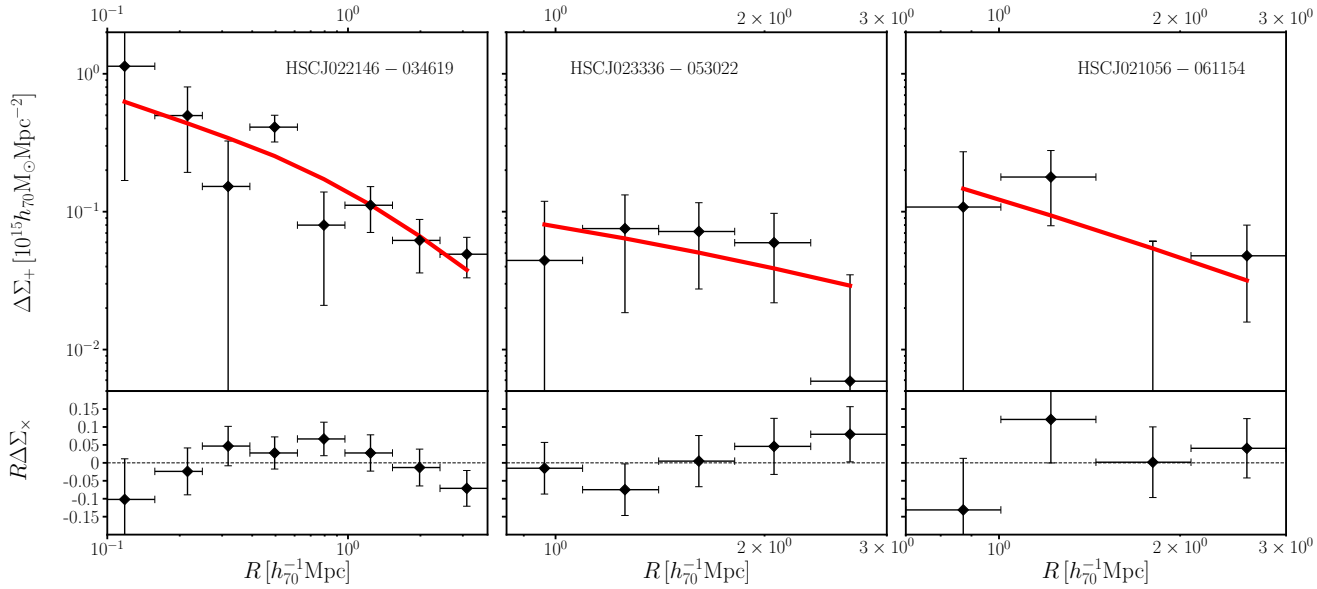


**Figure 4.** *Top*: Tangential shear profiles for the three subsamples of HSC J022146-034619, HSC J023336-053022, and HSC J021056-061154 (from left to right). *Bottom* : The product ($10^{15}h_{70}M_\odot\mathrm{Mpc}^{-1}$) of the 45 degree rotated component, $\Delta\Sigma_\times$, with the projected distance, $R$, as a function of $R$.

red galaxy distribution (Okabe et al. 2019) cannot find subhalos within $R_{200}$, two subhalo candidates can be expected by methodology. The first candidate is a subhalo within the smoothing scale of 200 kpc from the BCG and the second candidate is a less massive subhalo.

There is a second luminous galaxy at $(\alpha,\delta) = (35.4382, -3.7673)$ which is 106 kpc northwest from the BCG. Its stellar mass is about one-fourth that of the BCG. The presence of a second BCG is not rare in optical clusters. We perform the two-dimensional WL analysis using a single NFW model and its free central location. The resulting center is close to the second BCG rather than the BCG (Table 4 and Figure 6). Although the two galaxies are too close to resolve their mass structures by WL analysis, the position would be explained by the superposition of the mass associated with the second bright galaxy and the main halo. If the difference in their redshifts gives their relative peculiar velocity along the line of sight, $v = c\delta z/(1+z) \sim 450\,\mathrm{kms}^{-1}$ is likely to be subsonic motion. Therefore, the scenario that the moving second BCG triggers the hot component and sloshing pattern does not qualitatively contradict the observational results.

To search for a second halo candidate, we next made a galaxy number map of red and blue galaxies selected by

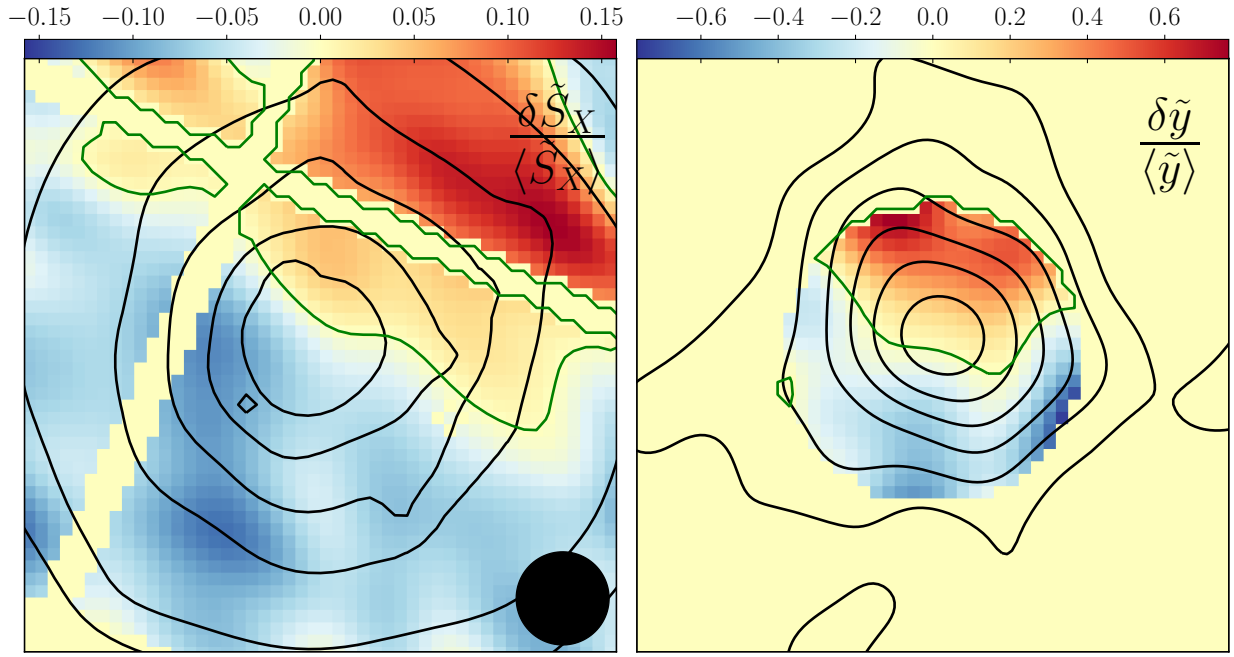


**Figure 5.** Fractional residual maps of the X-ray surface brightness (left) and the $y$ parameter (right) of the box of 2 arcmin × 2 arcmin of HSC J022146-034619, centering with the XXL center. *Left*: the residual $S_X$ map as computed from MOS1 and MOS2. The CCD gaps are evident as a cross pattern. Green contours are $\delta\tilde{S}_X = 0$. The black circle at the lower right corner shows the FWHM circle of the smoothing scale ($\sigma = 8$ arcsec) in order to reduce noisy feature. Black contours is $\tilde{S}_X$ distribution which is the same as in the top-middle panel of Figure 1. *Right*: the residual $y$ map on the XMM grid of 2.5-arcsec pixels. The map is masked outside $\theta = 0.5$ arcmin where $\tilde{y}$ is of low signal/noise. The smoothing is applied as in the left panel. Green contours are $\delta\tilde{y} = 0$. Black contours are the $\tilde{y}$ distribution which is as in the top-left panel of Figure 1.

**Table 3.** WL masses. †: mass computed from 2D WL analysis. ‡: shape catalogue in the central region is not available.

| Name | $M_{200}$ $[10^{14}\ h_{70}^{-1} M_\odot]$ | $M_{500}$ $[10^{14}\ h_{70}^{-1} M_\odot]$ |
|---|---|---|
| HSC J022146-034619 | $8.34^{+3.22}_{-2.49}$ | $5.69^{+1.65}_{-1.43}$ |
| HSC J023336-053022† | $2.46^{+1.27}_{-1.08}$ | $1.51^{+0.86}_{-0.71}$ |
| HSC J021056-061154‡ | $5.42^{+3.84}_{-3.84}$ | $4.30^{+3.01}_{-3.25}$ |

full probability function of the photometric redshift (Tanaka et al. 2018). Following Ichikawa et al. (2013) to map the surrounding galaxy distribution on the large scale, we compute a probability of each galaxy located at a slice of $\pm\Delta z$, defined by

$$p_{\rm gal} = \int_{z_l-\Delta z}^{z_l+\Delta z} P(z)dz \Big/ \int_0^\infty P(z)dz, \qquad (16)$$

where $P(z)$ is the full probability function, $z_l$ is a cluster redshift and $\Delta z$ is the redshift slice. Taking into account photometric redshift errors, we adopt $\Delta z = 0.1$ in a similar way to Eckert et al. (2017). The galaxy number distribution is shown in the right panel of Figure 7. The galaxy distribution is elongated along the north-south direction. The spectroscopically identified galaxies (Guglielmo et al. 2018) are shown by red pluses. A galaxy group is found around $(\alpha, \delta) = (35.4087, -3.8252)$ which is at $\sim 1.3$ Mpc south of the BCG. The group is mainly composed of red luminous galaxies. Diffuse X-ray emission is also found around $(\alpha, \delta) = (35.4269, -3.8115)$ which is $\sim 0.8$ Mpc south of the BCG and at $\sim 0.4$ Mpc north of the southern galaxy group. The X-ray contours along the line connected between the X-ray main peak and the southern X-ray emission is slightly curved outwards. One of possible interpretations is that the subhalo passed through the cluster center and gas was stripped away by ram-pressure. Since the southern galaxy group is compact and less massive, we measure its projected mass following a subhalo mass measurement (Okabe et al. 2014b). The projected mass, $M_{\zeta_c} = 3.5 \pm 0.8 \times 10^{13} M_\odot$, is only about 1/25 of the main halo.

Since having a less massive halo fall into a cluster occurs fairly often we cannot make a conclusive statement about which subhalo triggered the sloshing mode. Systematic future spectroscopic observations will reveal the details.

#### *4.1.3 Comparison with numerical simulations*

ZuHone et al. (2010) studied sloshing features in the gas core using $N$-body/hydrodynamic numerical simulations for which data is publicly available (ZuHone et al. 2018). We compute mock residual maps of simulated clusters at the

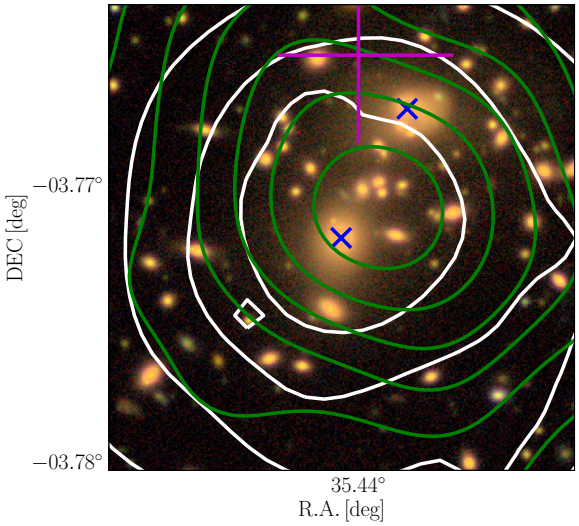


**Figure 6.** Optical *riz*-color image around the BCG of HSC J022146-034619 (1 arcmin × 1 arcmin). The white and green contours denote $y$ and $S_x$ distributions (Figure 1). The blue crosses represent the central BCG and the second brightest galaxy at the northwest. The large magenta symbol marks the WL-determined center and its error.

cluster redshift considering the PSFs and the transfer function. We use the data-set of $M_{200} = 10^{15} M_\odot$ for the main cluster and a subhalo with mass ratio 1 : 20 and impact parameter of 200 kpc. The sloshing modes appeared in any phases after the first impact. The direction of residual emission and pattern are affected by the viewing angle. We pick a phase at 2.5 Gyr after the closest encounter as a typical example. At this phase, the subhalo is on its way to the second impact after turn-around. Figure 8 is an edge-on view from the merger plane for the simulated $S_X$ and mass distributions. The subhalo is located at the south and a tailed gas feature is found. Inset figures are the fractional residual maps convolved with the PSFs and the transfer function excluding any observational noise. The coherent residual patterns and the location of the subhalo are similar to our observation ( Figures 5 and 7).

### 4.2 HSC J023336-053022

#### *4.2.1 Joint analysis*

The $y$ map shows a clear double-peaked structure associated with galaxy concentrations (the middle horizontal panel of Figure 1). An X-ray core with a round shape is found at the intermediate position between the two high $y$ components. The X-ray core can be visually decomposed into two substructures. The X-ray peak coincides with the positions of the eastern $y$ and galaxy structures. The secondary X-ray peak is located close to a surface-brightness weighted centroid. The $y$ parameter around the X-ray morphological center is lower than those of the double-peaked $y$ components. The high density and low pressure suggests that the X-ray core is likely to be a cool core. A possible scenario explaining the observed feature is that two clusters with cool cores are colliding with each other and two shock-heated regions are triggered ahead of the gas cores. The cluster is likely to be at a phase just after core passage.

As a first attempt at modeling, we assume a spherically symmetric gas distribution in a similar way as the other clusters (Secs 4.1 and 4.3), though the $y$ and $S_X$ distributions are composed of the three gas components. The azimuthally-averaged $y$ profile (the top-left panel of Figure 9) is almost constant at small radii and steeping at $\theta \sim 1$ arcmin because of the angular transfer function. For this cluster, we choose an X-ray count-rate weighted center within 100 kpc of the X-ray peak, because we find the $S_X$ and $y$ profile centers are misaligned with the XXL center. As expected from the observed $y$ profile, the modeled pressure profile has a shallow slope. The electron number density shows a steeply decreasing function and agrees with the model-independent, deprojected electron number density. The temperature profile slightly increases as the radius increases to compensate for the steep function of the electron number density.

In order to quantify the merger phenomena, we next consider three gas components as a function of three-dimensional space, $\boldsymbol{x}$,

$$g(\boldsymbol{x}) = g^{\rm C}_{\rm gNFW}(\boldsymbol{x}^{\rm C}_c; \boldsymbol{x}) + g^{\rm W}_{\beta}(\boldsymbol{x}^{W}_c; \boldsymbol{x}) + g^{\rm E}_{\beta}(\boldsymbol{x}^{E}_c; \boldsymbol{x}), \qquad (17)$$

where $g = n_e$ or $g = T_e$ and $\boldsymbol{x}_c$ is the central position. The subscript and superscript denote the type of models and central positions, respectively. We adopt the gNFW model for the central gas component in order to express the presence of the cool core. In order to describe the western or eastern hot-thin region, we adopt the $\beta$ model for simplicity. Since the outer slopes of the number density and temperature of the two hot regions cannot be constrained well, we fixed a slope $\beta_n = \beta_T = 1$. The slope is much steeper than a typical value of clusters derived by X-ray surface brightness profile (e.g. Pacaud et al. 2016, $\beta \sim 0.67$) in order to describe the gas locally heated by cluster merger shocks. We also assume that the scale radii of the western and eastern components are same. In other words, a difference between the western and eastern gas properties is described by the central temperature and density values.

When we compute the projected $y$ and $S_X$ distributions, we assume that the two gas components do not interact with each other. We treat central positions as free parameters, restricted to boxes of 1 arcmin × 1 arcmin centered on the brightest cluster galaxies of the western and eastern components and the cool core for the $W$, $E$ and $C$ components, respectively. We use two-dimensional images binned by ten pixels and four pixels for the $y$ and $S_X$, respectively. The pixel sizes of the binned images corresponds to 10 arcsec.

The resulting model maps and parameters are shown in Figure 10 and Table 2, respectively. The best-fit centers are shown in Table 4. The model maps do not take into account the transfer function and the PSFs to understand physical properties. The models succeed in reproducing the double-peaked distribution of the $y$ distribution (top-left panel) and the single cool core (middle and bottom panels). The emission-weighted, projected temperature of the central cluster component changes from $\sim 2$ keV at the cool core to $\sim 7$ keV at an intermediate radius of 2.5 arcmin. The temperature within 300 kpc from the best-fit centre

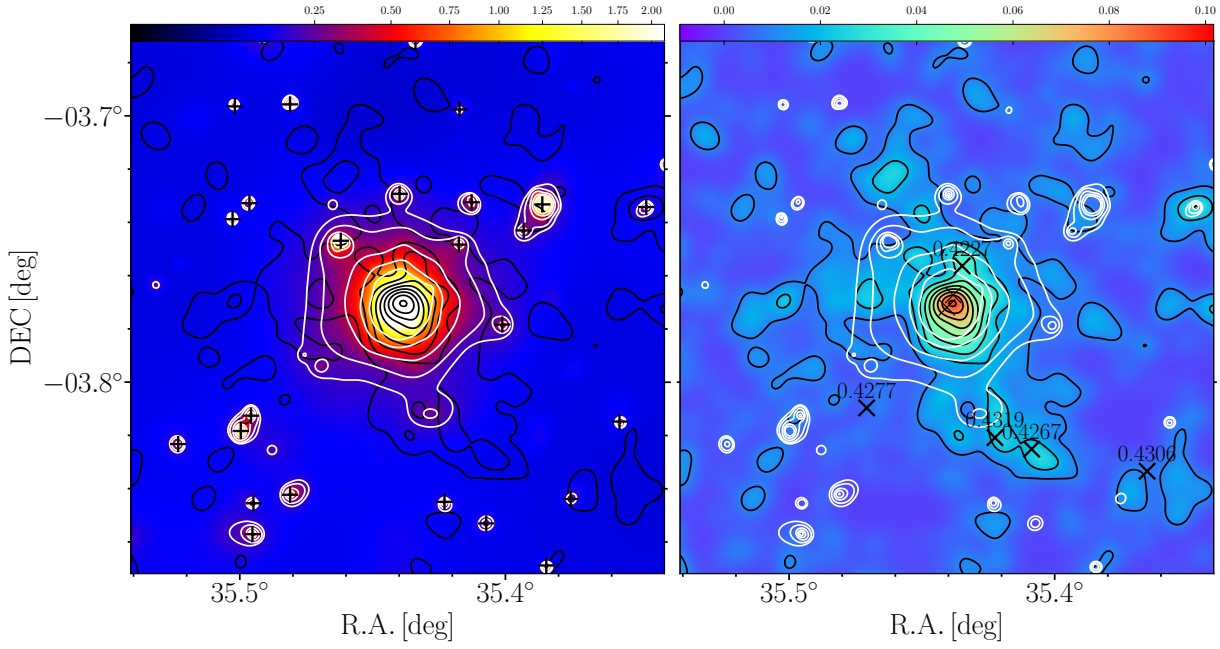


**Figure 7.** Adaptively smoothed X-ray map (left) and galaxy distribution (right) sliced by photometric redshift probability function $P(z)$. The full-width size is 12 arcmin. *Left*: the X-ray tailed feature from the cluster center to the southern region is marginally found. Black pluses denote X-ray point sources or foregrounds identified by cross-matching optical and X-ray images. White and black contours are X-ray and galaxy distributions, respectively. *Right*: the galaxy number density distribution smoothed with FWHM=200 kpc. Black X points are spectroscopically identified galaxies of which redshifts are shown in black texts, excluding the BCG and second bright galaxy. The galaxy distribution is elongated along the north and south direction on large scale. X-ray faint galaxy substructure is found around (35.4087,-3.82514). If the galaxy substructure were passing from the cluster center to the south, it could trigger the sloshing mode in the central region.

**Table 4.** Centers determined by two-dimensional fitting analyses.

| Component | $\alpha$ [deg] | $\delta$ [deg] |
|---|---|---|
| HSC J022146-034619 | | |
| Gas | $35.4389^{+0.0001}_{-0.0001}$ | $-3.7705^{+0.0001}_{-0.0001}$ |
| Mass | $35.4400^{+0.0029}_{-0.0034}$ | $-3.7653^{+0.0041}_{-0.0032}$ |
| HSC J023336-053022 | | |
| Gas C | $38.4081^{+0.0009}_{-0.0010}$ | $-5.5052^{+0.0014}_{-0.0010}$ |
| Gas W | $38.3889^{+0.0007}_{-0.0010}$ | $-5.5053^{+0.0004}_{-0.0004}$ |
| Gas E | $38.4153^{+0.0020}_{-0.0007}$ | $-5.5016^{+0.0006}_{-0.0005}$ |
| Mass W | $38.3895^{+0.0058}_{-0.0072}$ | $-5.5030^{+0.0051}_{-0.0068}$ |
| Mass E | $38.4178^{+0.0067}_{-0.0103}$ | $-5.5069^{+0.0062}_{-0.0070}$ |
| HSC J021056-061154 | | |
| Gas E | $32.7338^{+0.0010}_{-0.0035}$ | $-6.1975^{+0.0010}_{-0.0009}$ |
| Gas W | $32.7208^{+0.0021}_{-0.0035}$ | $-6.1998^{+0.0018}_{-0.0027}$ |
| Ell Gas E | $32.7358^{+0.0022}_{-0.0015}$ | $-6.1978^{+0.0007}_{-0.0008}$ |
| Ell Gas W | $32.7228^{+0.0009}_{-0.0011}$ | $-6.2003^{+0.0013}_{-0.0015}$ |

agrees with expected by the WL mass (Sec 4.6). Although the temperature of the intermediate radius is slightly higher than expected from the WL mass, $\tilde{y}$ at the radius is negative due to the transfer function. The temperature measurement at the radius leave for future work. The emission-weighted projected temperatures within the projected radius 300 kpc from the best-fit centres in the western and eastern regions are $\sim$ 30 keV and $\sim$ 20 keV, respectively. We note that a relativistic correction is small in the observing frequency (e.g. Hughes & Birkinshaw 1998; Mroczkowski et al. 2019). Their temperatures are three or four times higher than that of the cool component in the same regions. However, the electron number density of the two hot regions is lower than that of the cool component. We compute the integral of the electron density over a cylindrical volume within a projected radius 300 kpc from the best-fit central position of the western/eastern component. The ratios of the electron number of the western/eastern component to the total component are 0.45/0.38, respectively. It thus indicates that a small fraction of the ICM is locally heated by the cluster merger. If we assume that the outer slopes for the hot component is $\beta = 2$, the projected temperatures in the western and eastern components become higher by $\sim$ 20 per cent and lower by $\sim$ 10 per cent, respectively.

To measure cluster richnesses of the western and eastern components we split into two galaxy components by right ascension of a bright galaxy ($\alpha = 38.3991$) around the cool core. Based on the S16A catalogue (Aihara et al. 2018b; Oguri et al. 2018), the richness of the western and eastern galaxies are 25 and 14, respectively. The total stellar masses are $M_*^{\rm W} = 3{\times}10^{12} M_\odot$ and $M_*^{\rm E} = 10^{12} M_\odot$. When we use the S18A catalogue (Aihara et al. 2019), the result does not significantly change; $M_*^{\rm W} = 3{\times}10^{12} M_\odot$ and $M_*^{\rm E} = 2{\times}10^{12} M_\odot$. Since cluster richness and halo mass are positively correlated

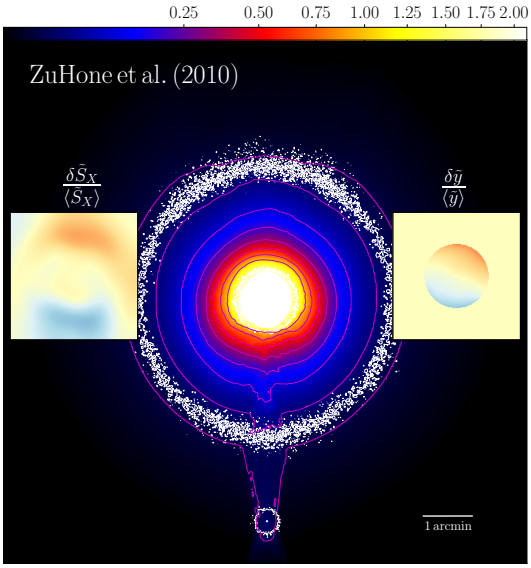


**Figure 8.** One of examples of simulated sloshing images retrieved from ZuHone et al. (2010, 2018). White and magenta contours are projected mass and X-ray surface brightness distributions, respectively. Inset panels are fractional residual $\tilde{S}_X/\langle\tilde{S}_X\rangle$ (left) and $\tilde{y}/\langle\tilde{y}\rangle$ maps (right) taking account of the PSFs and the transfer function of the box of 2 arcmin × 2 arcmin. The appearance of the residual images resembles our residual images (Figure 5). The configurations of the X-ray and mass clumps are similar to those in Figure 7.

(Okabe et al. 2019), the western galaxy component is likely to be the main cluster.

We measure weak-lensing mass assuming a tangential shear profile (Figure 4) and a two-dimensional weak-lensing analysis similar to that used to measure multi-component masses in other merging clusters (Okabe et al. 2011, 2015; Medezinski et al. 2016). Since the concentration parameters of the two halos and the mass of the subcluster are ill-constrained (because of a small number of background galaxies), we assume the mass-concentration relation in Diemer & Kravtsov (2015). The central positions of the two halos are treated as free parameters in a similar way as the two-dimensional SZE and X-ray analysis.

We first fit with uniform priors and obtain $M^W_{200} = 1.28^{+1.17}_{-0.65} \times 10^{14} h^{-1}_{70} M_\odot$ and $M^E_{200} < 0.75 \times 10^{14} h^{-1}_{70} M_\odot$. This indicates that the western component is the main cluster, consistent with the richness. The central positions determined by WL analysis, shown in Table 4, coincide with BCG positions of the two galaxy components. Since we give an upper limit of the mass of the eastern component, we repeat fitting with fixed centers at best-fit positions. The individual halo masses are $M^W_{200} = 1.54^{+1.29}_{-0.66} \times 10^{14} h^{-1}_{70} M_\odot$ and $M^E_{200} = 0.90^{+0.99}_{-0.40} \times 10^{14} h^{-1}_{70} M_\odot$. The best-fit mass ratio between the subcluster and the total cluster is roughly 2 : 3. Considering the error matrix, the mass ratio is $0.54^{+0.93}_{-0.28}$. The resulting matter distribution is shown by the red lines in Figure 10. Even when we fit the entire shear pattern with single NFW model, the best-fit center is consistent with the western BCG position rather than the eastern BCG position, indicating that the western component is the main cluster.

### *4.2.2 Merger dynamics*

The $y$ and $S_X$ distributions (Figure 1 and 10) show violent merger phenomena, indicating that the merger is at the phase just after core-passage. The morphological information suggests that the cluster merger event mainly occurs in the sky plane even though there is a line of sight motion.

We estimate the merger time-scale after core passage. Since dark matter is likely composed of collisionless particles, the WL-determined central position can constrain the merger timescale (Okabe et al. 2011, 2015). From the two-dimensional WL analysis (Sec 4.2), assuming a point mass approximation, the projected distances between the two clusters and between the subhalo and the center-of-mass are estimated to be $\sim 580$ kpc and $\sim 370$ kpc, respectively. Okabe et al. (2019) found a segregation in a probability density function (PDF) of collision velocities of the optically-defined merging clusters and well-known merging clusters with diffuse synchrotron radio emissions. The peak velocities of the optically-defined merging clusters and merging clusters with diffuse radio emissions are $\sim 1000\,\mathrm{km\,s^{-1}}$ and $\sim 2500\,\mathrm{km\,s^{-1}}$, respectively. The former and latter cases give the merger timescales after core passage of $\sim 0.36$ Gyr and $\sim 0.14$ Gyr, respectively.

We also estimate merger velocity from the deviation from a mass-temperature scaling relation (Lieu et al. 2016). Assuming that the gas temperature before the merger follows the mass-temperature scaling-relation (see details in Sec. 4.6), we infer a pre-merger temperature from the eastern WL mass, and derive a Mach number, $\mathcal{M}^E \sim 6.2$, from the ratio between the eastern hot and pre-merger temperatures. The resulting collision velocity is $v^E \sim 3900\,\mathrm{km\,s^{-1}}$ with the sound velocity of $c_s \sim 640\,\mathrm{km\,s^{-1}}$ expected by the WL mass. Thus, the merger time-scale is $\sim 0.16$ Gyr, assuming a one-dimensional velocity of $v^E/\sqrt{3}$. A difference between spectroscopic redshifts (Guglielmo et al. 2018) of two luminous galaxy associated with the western and eastern structure gives a relative velocity of $\delta v_{\rm l.o.s} \sim 1700\,\mathrm{km\,s^{-1}}$. If the subhalo is not moving along the Dec direction, the time-scale is $\sim 0.1$ Gyr with $((v^E)^2 - \delta v^2_{\rm l.o.s})^{1/2} \sim 3500\,\mathrm{km\,s^{-1}}$. Even when we use a mass-temperature scaling relation (Umetsu et al. 2019), the estimated time-scale does not significantly change. The estimated collision velocity is acceptable in cosmological simulations (Bouillot et al. 2015) and observations (Okabe et al. 2019), but is at high end of the PDF of collision velocities for the optically-defined merging clusters and similar to those of merging clusters with diffuse radio emission.

### *4.2.3 Comparison with numerical simulations*

In order to visually interpret merger phenomena, we made simulated MUSTANG-2 and *XMM-Newton* images using the numerical simulations of ZuHone (2011) publicly available through ZuHone et al. (2018). ZuHone (2011) computed $N$-body/hydrodynamic simulations of binary mergers with mass ratios of 1 : 1, 1 : 3 and 1 : 10 with impact parameters of 0, 500 and 1000 kpc. The main cluster mass is $6 \times 10^{14} M_\odot$,

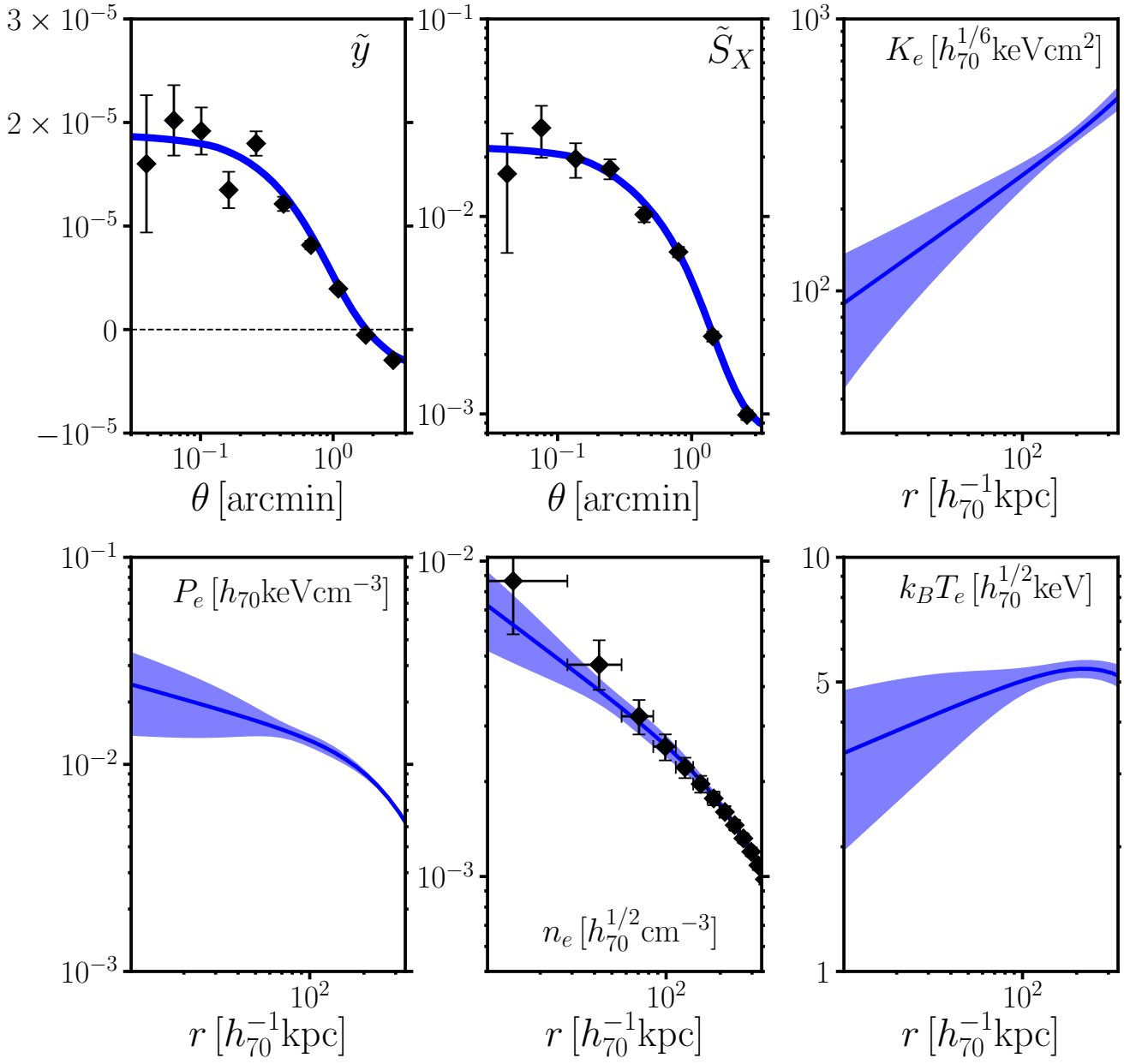


**Figure 9.** The same figure as Figure 3, but for HSC J023336-053022. The signal-to-noise ratios of the $\tilde{y}_d$ and $\tilde{S}_{Xd}$ profiles are $\sim 36\sigma$ and $\sim 24\sigma$, respectively.

which is slightly higher than those of our samples. We set simulated clusters at the observed redshifts of the merging cluster and then pick out a simulated cluster so that their peak separations between $y$ and $S_X$ maps measured from 90 deg from the merger plane are similar to our observations. The dynamical time and mass ratio are close to our cases. The simulated images, convolved with the PSFs and the transfer function, are shown in Figure 11. The X-ray merger positions are rotated to be along the $x$-axis. The upper panel of Figure 11 shows the $\tilde{y}$ and $\tilde{S}_X$ maps of an equal-mass merger with zero impact parameter. The simulated images of the $y$ parameter clearly show a double-peaked structure. Bow-shock fronts (red lines) are located at outer-edges of the two hot components. These bow shocks appear as weak changes in the $y$ map. We find that it is difficult to constrain the Mach number from the $y$ distribution. The $y$ peak regions are heated by cluster merger shocks ($\mathcal{M} \sim 4.7$). In the simulations, the temperature in these regions reaches $\sim 25$ keV from the initial value $\sim 5$ keV, support the presence of the hot-component in the major merger. The X-ray core is located between the two peaks in $y$, which is overall consistent with our observation. The observed peak X-ray core is

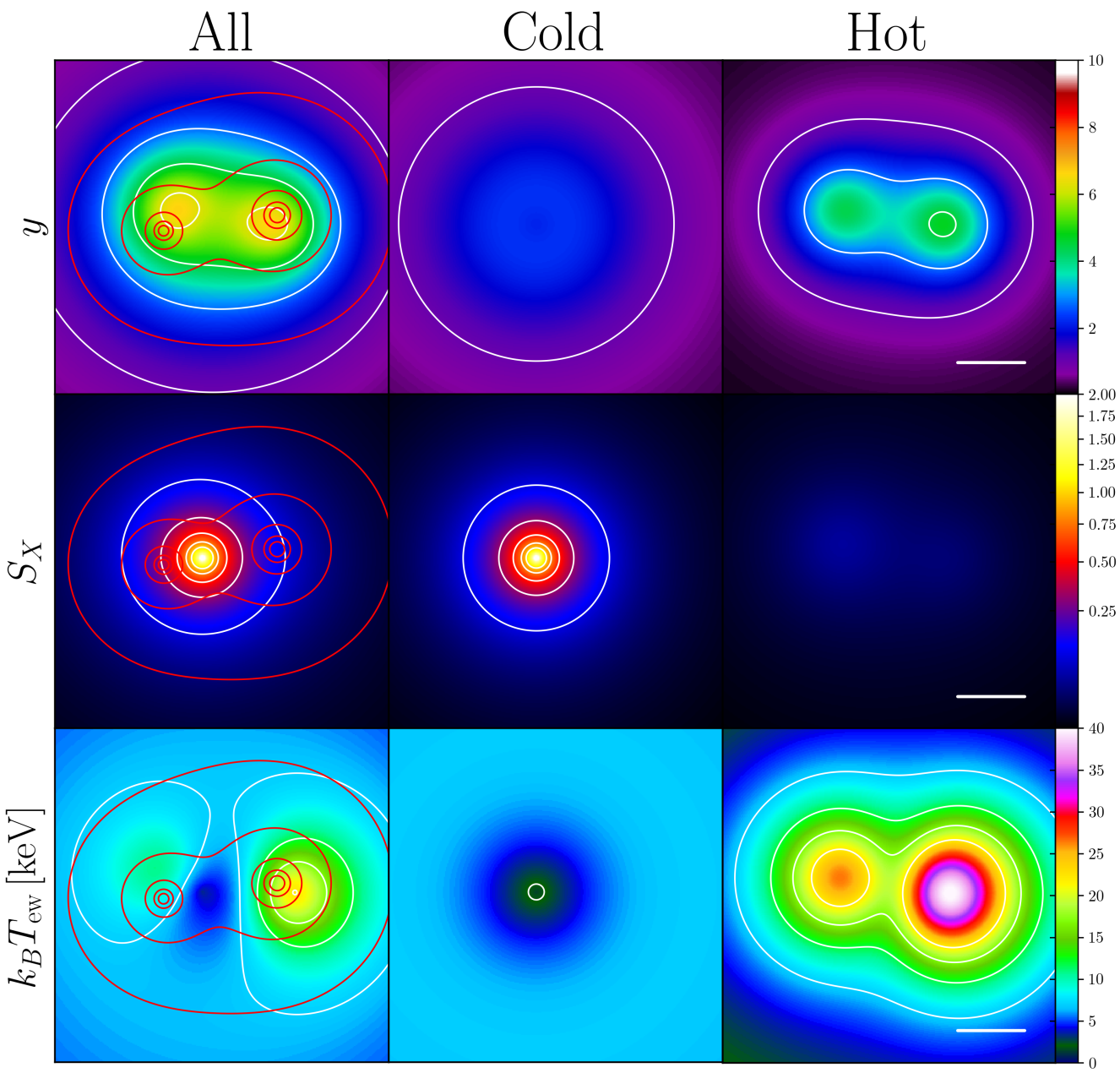


**Figure 10.** Model maps for HSC J023336-053022: $y$ map [$10^{-5}$] (*Top*), $S_X$ map in arbitrary units (*Middle*), and emission-weighted temperature, $k_B T$ [keV] (*Bottom*). The full-width size is 5arcmin. Neither the transfer function nor the PSF has been applied. From left to right, the panels show the total gas components, the cold gas component, and the hot gas component, respectively. The red contours denote the projected mass contours derived by two-dimensional WL analysis ($[0.1, 0.3, 1.1, 2.3, 4] \times 10^{14} M_\odot$ Mpc$^{-2}$, stepped by square root). The white lines shown in the right panels denote 1 arcmin.

located close to the eastern $y$ component, which might indicates that this is an unequal mass merger. Indeed, in the simulation (ZuHone 2011) of a less massive subcluster (1/3) than our case (2/3), the stripping core is associated with the subcluster.

We stress that the joint SZE and X-ray analysis using high-angular resolution data provides a powerful means to extract the multiple gas structures and uncover hot components with $k_B T \sim 20 - 30$ keV. Such spatially-resolved high temperature measurements are difficult with current X-ray satellites. Future *Chandra* observations will test our interpretation by detecting the X-ray surface brightness jumps as shown in red curves in the upper panel of Figure 11, and will independently estimate the Mach number.

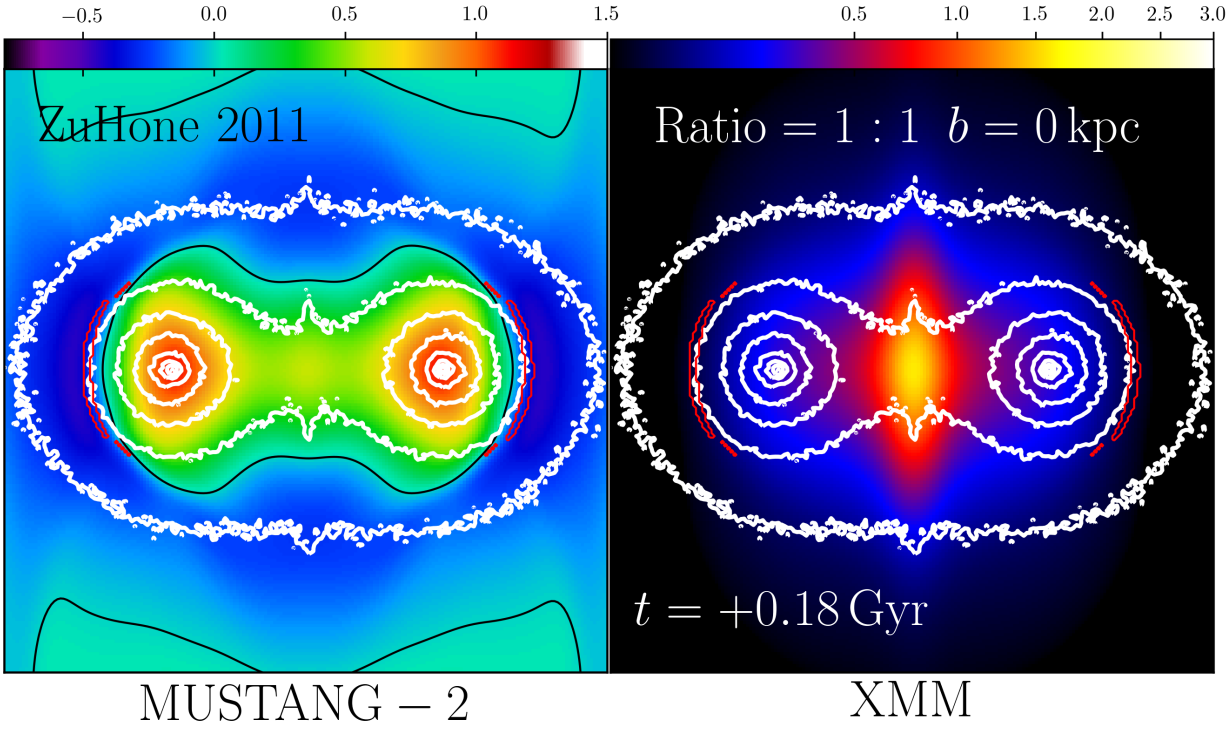


**Figure 11.** Simulated MUSTANG-2 (left) and *XMM-Newton* (right) images (4 arcmin × 4 arcmin) using numerical simulations of ZuHone (2011) publicly available through ZuHone et al. (2018), taking into account the PSFs and the transfer function. The panels are the edge-on view of a binary merger with equal-mass ratio and impact parameter $b = 0$ kpc at 0.18 Gyr after first core-passage, which is similar to the case of the major merger, HSC J023336-053022. The white contours denote projected mass density. The black contours in the left panels denote the lines for $\tilde{y} = 0$. The red lines are shock features appearing in the projected sky.

#### *4.2.4 No diffuse radio emission*

The major-merger candidates defined by Okabe et al. (2019) evenly cover a new parameter region of mass, mass ratio, and dynamical stages. One main difference from well-known mergers with diffuse synchrotron radio emissions, so-called radio halos and relics, is that the PDF of the merger velocity of the optically defined mergers is shifted to lower speeds. Okabe et al. (2019) found no diffuse radio emission in $\sim 190$ merging clusters by both visual inspection and spectral index maps using the NVSS (1.4 GHz; Condon et al. 1998) and TGSS (147.5 MHz; Intema et al. 2017) archival data because it is very difficult to discriminate between radio lobes and halos/relics. Combined with a presence of hot regions revealed by joint SZE and X-ray analysis, it is a good opportunity to search again for radio halos/relics in the major-merging cluster.

We here use the FIRST (1.4GHz; Helfand et al. 2015) data and the GMRT data of the XXL Survey (610MHz; Smolčić et al. 2018). The beam sizes for the FIRST and GMRT data are 5 arcsec and 6.5 arcsec, respectively. In the FIRST image we find a point source (FIRST J023334.1-053008) associated with a bright cluster galaxy at spectroscopic redshift $z = 0.4319$ in the western component of the cluster (Figure 12). The SZE flux around the radio source is suppressed by compact radio source contamination. The radio contamination depends on the spectral index at high frequency (e.g. Gralla et al. 2014). We note that the radio source region is excluded in the modeling fitting. At 610 MHz (Smolčić et al. 2018) there are three sources (XXL-GMRT J023339.6-053028, XXL-GMRT J023334.1-053008, and XXL-GMRT J023332.1-053008). One of them coincides with the source listed in the FIRST catalogue; the three radio sources are associated with cluster members (right panel of Figure 12). The radio AGN activity might be recently triggered by the cluster merger ($\sim 0.15$ Gyr) because the typical timescale of AGN activities is short $0.01 - 0.1$ Gyr (Soker 2016).

We do not significantly find diffuse radio sources, though the SZE and X-ray data exhibit the presence of hot gas components triggered by the violent merger. This conflicts with the other cases of CIZA J2242.8+5301 (van Weeren et al. 2010) hosting a prominent filamentary radio relic, Abell 2146 (Hlavacek-Larrondo et al. 2018) with double relics, and the bullet cluster (Markevitch et al. 2002) with a radio halo. The estimated merger timescale is comparable to $\sim 0.1 - 0.2$ Gyr for the bullet cluster (Markevitch et al. 2002), and $0.2 - 0.3$ Gyr for CIZA J2242.8+5301 and Abell 2146. One of differences is cluster mass. CIZA J2242.8+5301 (Okabe et al. 2015), Abell 2146 (King et al. 2016), and the bullet cluster (Bradač et al. 2006) are very massive ($M_{200} \sim 10^{15} h_{70}^{-1} M_\odot$), while the mass of this cluster is only one-tenth that ($M_{200} \sim 10^{14} h_{70}^{-1} M_\odot$). Thus, the release of gravitational energy differs by more than one order of magnitude. Cassano et al. (2013) have shown that the $k$-corrected radio power at 1.4 GHz for diffuse radio emissions have a strong mass dependence; $P_{1.4\mathrm{GHz}} \propto M_{500}^{p}$ with $p = 3.77 \pm 0.57$. The upper limit of $P_{\mathrm{FIRST}} \sim 3 \times 10^{23}$ W Hz$^{-1}$

with $3\sigma$ level is higher than $0.5 \times 10^{23}\,\mathrm{W\,Hz^{-1}}$ expected by the relation of Cassano et al. (2013) using the WL mass, and thus we do not rule out a possibility to detect diffuse radio emission by future observations with 1.4 GHz. Assuming the spectral index $\alpha = 1.3$ (Cassano et al. 2013), the expected radio powers at the GMRT and TGSS frequencies are $\sim 2 \times 10^{23}\,\mathrm{W\,Hz^{-1}}$ and $\sim 10^{24}\,\mathrm{W\,Hz^{-1}}$, respectively. The $k$-corrected powers of the $3\sigma$ rms noise levels of the GMRT and TGSS observations are $\sim 10^{23}\,\mathrm{W\,Hz^{-1}}$ and $\sim 4 \times 10^{24}\,\mathrm{W\,Hz^{-1}}$, respectively. Therefore, expected diffuse radio sources (Cassano et al. 2013) are not detected by the GMRT observation (Smolčić et al. 2018).

Thanks to the multi-component gas analysis and high-angular resolution synchrotron radio data, we can constrain the upper limit of the particle acceleration efficiency $\eta_e$ via the first-order Fermi acceleration. We assume that a merger shock created the hot gas component and simultaneously injected cosmic-ray electrons. An injection spectra at downstream of the shock is defined by $Q_e = Q_{e,0}\gamma^{-p}$, where $p$ is the particle index, $\gamma$ is the Lorentz factor, and $Q_{e,0}$ is the injection normalization. Assuming a diffusive shock acceleration (DSA; Drury 1983), the particle index is given by $p = 2(\mathcal{M}^2+1)/(\mathcal{M}^2-1)$. Cluster merger shocks convert kinetic energy to thermal energy. The total thermal energy of electrons heated by the merger shock can be computed from the pressure of the hot gas component measured by the multi-component analysis, $E_{\mathrm{th},e} = \int (3/2) P_e dV$. When we constrain the upper limit of the acceleration efficiency, we assume that all the kinetic energy is converted to the thermal energy. The injection energy is described by $\int_{\gamma_{\min}} Q_{e,0}\gamma^{-p} E d\gamma = \eta_e E_{\mathrm{th,e}}/\Delta t$ using a constant efficiency factor $\eta_e$, where $\Delta t$ is the merger time scale and $E$ is the energy per a cosmic ray electron. We assume $\gamma_{\min} = 2$. Given the injection spectra and the inverse-Compton and synchrotron energy losses, the steady state spectra has a form of $N(\gamma) \propto \gamma^{-(p+1)}$ (Sarazin 1999). Then, the synchrotron emissivity is $dL_{\mathrm{syn}}/d\nu \propto B^{(p+2)/2}\nu^{-p/2}$, where $B$ is the magnetic field strength and $\nu$ is a frequency. A cooling time scale for cosmic-ray electrons emitting at the GMRT frequency is 0.04 Gyr assuming a typical magnetic field $B = 1\,\mu G$ and shorter than the merger time scale $\sim 0.15$ Gyr. We assume Mach number $\mathcal{M} = 6.2$ and $\Delta t = 0.16$ Gyr (Sec. 4.2.2). Even when we change by $\mathcal{M} = \pm 2$ or $\Delta t = \pm 0.05$, the results do not significantly change. We consider the cylindrical volume of the eastern hot component within the central 1 arcmin. The left panel of Figure 13 shows a comparison of the $1\sigma$ upper limits of the radio observations and the synchrotron flux density expected by 0.3, 1 and 3 percent acceleration efficiency at $B = 1\,\mu G$. The upper limits of the radio observations are estimated by the $3\sigma$ level. The acceleration efficiency should be less than $\mathcal{O}(10^{-2})$, which is lower than typical in theoretical models of galaxy clusters (e.g. Kang & Ryu 2013; Vazza et al. 2016) and strong shocks in supernova remnants (e.g. Miniati et al. 2001). The right panel of Figure 13 shows the upper limit on $\eta_e$ as a function of $B$. Since magnetic strengths of order of $\mathcal{O}(1)\,\mu G$ (e.g. Vogt & Enßlin 2003) or higher in radio relics (Nakazawa et al. 2009; van Weeren et al. 2011), the acceleration efficiency is less than sub percent and thus is very inefficient. Similar results are recently reported in well-known radio-relic clusters (Botteon et al. 2019).

Another possibility for particle acceleration is re-acceleration of supra-thermal electrons which are possibly ejected from AGN radio sources. If the AGN sources were not lightened before merger shocks was sweeping, the scenario would not conflict with non-detection of diffuse radio sources, given their short time cycles of $0.01-0.1$ Gyr (Soker 2016).

### 4.3 HSC J021056-061154

#### *4.3.1 Joint analysis*

HSC J021056-061154 exhibits a complex distribution of member galaxies, comprising a central component elongated along the west-east direction and southern substructures (the bottom-right panel of Figure 1). The central X-ray surface distribution is elongated along the east-west direction, similar to the central galaxy distribution. The X-ray peak position coincides with the BCG position. The X-ray flux is much lower than that of the other clusters. The bottom-left panel of Figure 1 shows an anisotropic distribution of the Compton $y$ parameter. The eastern and western regions show negative and positive $y$ values, respectively. The high $y$ region is elongated along the direction perpendicular to the major axis of the X-ray core. Taking into account the angular transfer function, this feature indicates that the peak position of the $y$ parameter, that is, the hot region, is offset 45 arcsec to the west of the BCG.

Figure 14 shows the $y$ and $S_X$ radial profiles. The signal-to-noise ratio of the $y$ profile is much lower than those of the other clusters. Since it is difficult to constrain the outer-slope, we adopt a Gaussian prior $\beta_T = 0.67 \pm 0.30$ for the modeling. The temperature is an increasing function out to $\sim 500$ kpc. When we refit with the constant temperature model, the model is disfavored to describe the $\tilde{y}$ profile. The measurement uncertainty of the temperature is larger than that of the electron number density because of the low signal-to-noise ratio of the $y$ profile.

We next perform the two-dimensional analysis in a similar way to Sec 4.2. Since the signal-to-noise ratio is low, we use the binned images with pixel size of 20 arcsec. In modeling, we consider the eastern and western components to describe the main cluster and the offset hot component, respectively. We adopt the spherically symmetric gNFW model for the eastern main component and the spherically symmetric $\beta$ model for the western hot component. We fixed $\beta_n^{\mathrm{W}} = \beta_T^{\mathrm{W}} = 1$ to describe the localized hot component in a similar way to Sec 4.2. As shown in the lower-middle panel of Figure 15, the main cluster has a cool core in which the emission-weighted temperature changes from $\sim 3$ keV to $\sim 6$ keV as the radius increases. The emission-weighted temperature for the main component within 300 kpc from the XXL center is $\sim 5$ keV. The features of the main component are not significantly different from the results of the one-dimensional analysis. The western temperature reaches $\sim 11$ keV. The best-fit centers are shown in Table 4. The superposed temperature map (the lower-left panel of Figure 15) exhibits an anisotropic distribution. A small gas fraction of the western region has a high temperature, while the eastern region is not affected by the high temperature component. The feature indicates that the cluster is likely to be before the merger. The superposed X-ray surface brightness distribution is elongated along the east-west direction.

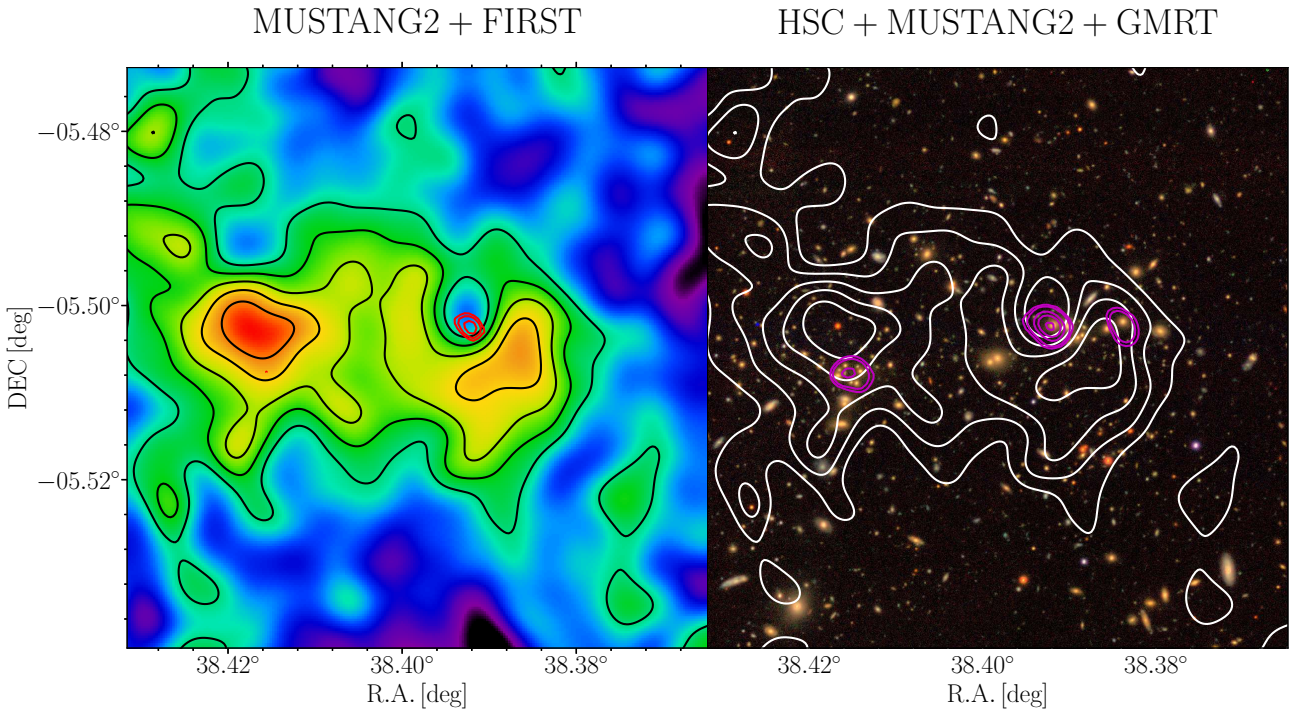


**Figure 12.** *Left:* the $y$ map for HSC J023336-053022 overlaid with the FIRST (red) contours (1.4 GHz). The contour levels are $4, 8, 16,$ and $32 \times \sigma_{\rm rms}$, where $\sigma_{\rm rms}^{\rm FIRST} = 1.5 \times 10^{-4}$ Jy beam$^{-1}$. *Right:* HSC-SSP optical $riz$-color image overlaid with the $y$ map contours (Figure 1) and the GMRT contours (magenta). The contour levels are $4, 8, 32, 64, 128,$ and $512 \times \sigma_{\rm rms}$, where $\sigma_{\rm rms}^{\rm GMRT} = 6 \times 10^{-5}$ Jy beam$^{-1}$. The three low-frequency radio sources are associated with member galaxies. The black contours in the left panel and the white contours in the right panel show the distribution of the Compton $y$ parameter (same levels as in Fig.1, left panel, second row).

Since the cluster is located at the edge of the HSC-SSP survey field, the shape catalogue does not fully cover the entire region of the cluster because of the full-colour and full-depth condition (Sec. 3.4). Therefore, the measurement uncertainty of the WL mass is very large (the right panel of Figure 4 and Table 3). We cannot carry out a multi-component WL analysis because of this limitation. A comparison of weak-lensing and HE-derived masses is discussed in Sec 4.8.

### *4.3.2 Pre-minor merger physics*

The $y$ map of this cluster (Figure 1) is chaotic in structure, with a peak offset to the west of X-ray peak. In particular, the major axis of the $y$ map is elongated perpendicular to that of the X-ray core. We adopt an elliptical model to describe the gas structure.

The ellipticity of the the projected distribution of the electron number density and temperature is defined by $e = 1 - b/a$, where $a$ and $b$ are the major and minor axes of gas properties following Oguri et al. (2010). We introduce an orientation angle of the major axis, $\phi_e$, measured from the north to the east. The distance of an iso-contour from the centre is given by

$$\begin{aligned} r &= (x'^2/(1-e) + (1-e)y'^2)^{1/2}, \qquad (18) \\ x' &= x\cos\phi_e + y\sin\phi_e, \\ y' &= -x\sin\phi_e + y\cos\phi_e, \end{aligned}$$

where $x'$ and $y'$ are the rotated coordinates. The best-fit orientation angles of the eastern and western components are $\phi_e^{\rm E} = 112^{+7}_{-8}$ deg and $\phi_e^{\rm W} = 17^{+9}_{-10}$ deg, respectively. The elongation of the hot gas in the projected sky is almost perpendicular to that of the cold gas. This suggests that the hot region has been heated by a merger shock triggered by the infalling dense gas. The ellipticities are $e^{\rm E} = 0.53^{+0.10}_{-0.13}$ and $e^{\rm W} = 0.29^{+0.16}_{-0.18}$. The best-fit model map is shown in Figure 16. Since the eastern region is not yet heated, the cluster is interpreted to be in a pre-merger phase.

We did not consider the elongation along the line of sight. Another possibility is that an ellipticity of the temperature distribution differs from that of the density distribution. If the temperature distribution were more elongated on the sky plane than the gas distribution, the $y$ parameter would be lower than expectations from the spherical model. A full three reconstruction of gas properties is left for future studies to address the geometrical assumption.

A group of several member galaxies in the west end of the central overdensity region is associated with the western hot region. The stellar mass of this group, $M_*^{\rm W} = 3 \times 10^{11} M_\odot$, is lower than the total stellar mass of $M_* = 4 \times 10^{12} M_\odot$ found using the S16A catalogue. When we use the S18A catalogue, our estimates become $M_*^{\rm W} = 7 \times 10^{11} M_\odot$ and $M_* = 4 \times 10^{12} M_\odot$. Therefore, the substructure mass triggering the hot region is one-tenth or less of the mass of the main cluster. The configuration and mass suggest that this system is likely to be a minor merger before core pas-

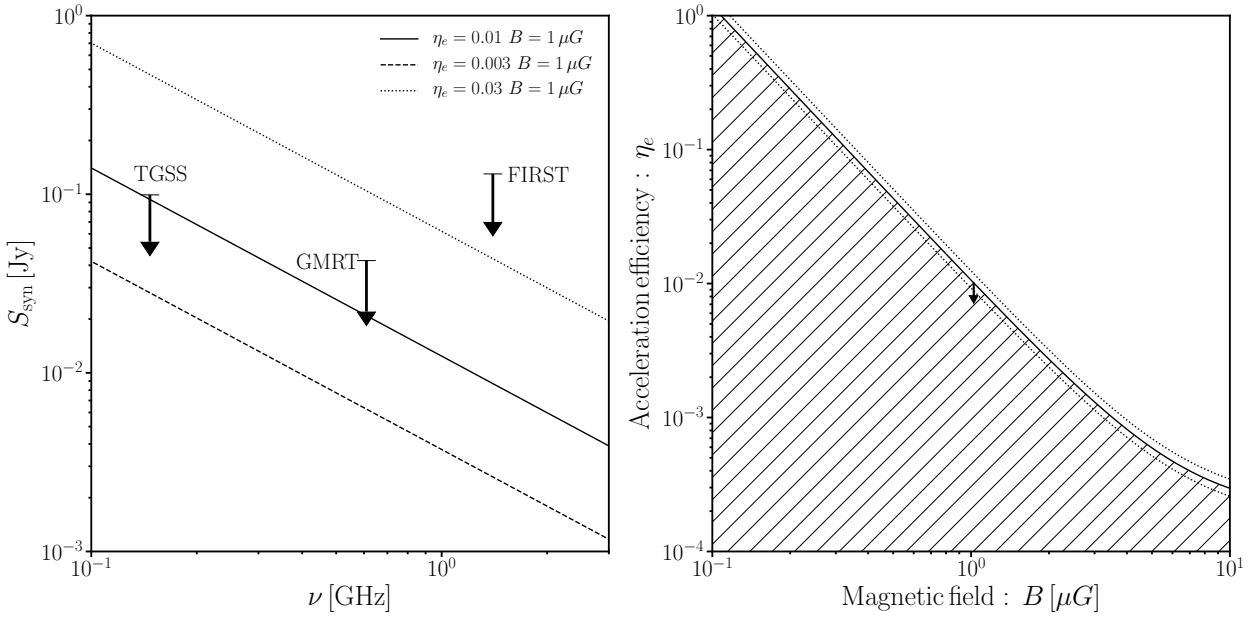


**Figure 13.** *Left*: synchrotron radio flux density. Radio upper limits are given by $3\sigma_{\rm rms}$ levels. The solid, dashed, and dotted lines are the radio flux density expected by the multi-component joint SZE and X-ray analysis with different acceleration efficiency, $\eta_e$. *Right*: the upper limits of the acceleration efficiency as a function of magnetic strength. The dotted lines denote the errors computed from the uncertainty of $P_e$. Non-detection of diffuse radio emission in the hot gas component gives the low acceleration efficiency of $< 10^{-2}$ at $B > 1\,\mu G$.

sage. Assuming a collision velocity of $1000\,{\rm km s^{-1}}$ (Okabe et al. 2019), the spatial separation of the two galaxy concentrations implies that the cluster is $\sim 0.3\,{\rm Gyr}(\sec\theta/1)$ before core passage. Here, $\theta$ is an inclination angle between the merger axis and the sky plane. The ratio between the projected temperatures of the hot and cold components gives the Mach number $\mathcal{M} \sim 4$ and the one-dimensional collision velocity $v/\sqrt{3} \sim 1500\,{\rm km s^{-1}}$ and the estimated time-scale, $\sim 0.2\,{\rm Gyr}$, is not significantly changed.

#### *4.3.3 Comparison with numerical simulations*

For visual purposes, we compute mock images using numerical simulations of ZuHone (2011) in a similar way of Sec. 4.2.3. Figure 17 shows an edge-on view of a simulated merger with 1 : 10 mass ratio and $b = 500$ kpc at $t = 0.14$ Gyr before first core-passage. The double-peaked X-ray surface brightness distribution and the elongated $y$ map associated with the western subcluster are found. The simulated $y$ map after processing with the transfer function, has negative values at $\theta \gtrsim 1$ arcmin. This morphology resembles the observation. The western component is heated by a merger shock (red lines). The simulated $y$ image shows a high value around the main cluster, while our observation does not detect such a feature, perhaps caused by a difference between an assumed cool core in numerical simulations and the observed cluster, and/or a different main cluster mass. Although the details of the simulated image are not identical to our image, the characteristic properties of the precursor phase of a minor merger well represents the observation.

### 4.4 Comparison with SZE and X-ray images in previous observations

We compare SZE and X-ray imaging for the three clusters with those reported from previous observations. As aforementioned, the high resolution mapping and their multi-wavelength analysis reveal that the gas properties are more or less disturbed regardless of the number of galaxy density peaks. Thus, even minor mergers along with galaxies or small subhalos which are not significantly detected by the peak-finding method (Okabe et al. 2019) trigger perturbations in distributions of gas temperature and density. The observed properties are summarized as follows. The single-peaked cluster shows the sloshing pattern in both the $y$ and $S_X$ distributions (Sec. 4.1.2). The double-peaked cluster with the mass ratio of $\sim 2 : 3$ has the single X-ray core between the two $y$ peaks (Sec. 4.2). The part of the supercluster exhibits the elongated hot region perpendicular to the major axis of the cool gas core (Sec. 4.3.2). Multi-wavelength results of SZE, X-ray, WL and optical measurements agree with predictions of the imaging patterns in numerical simulations (ZuHone et al. 2010; ZuHone 2011; ZuHone et al. 2018); the single-peaked cluster, the double-peaked cluster, and the part of the supercluster are likely to be at sloshing, post-major, and pre-minor merging phases, respectively.

Sloshing features are found in many clusters through X-ray observations (e.g. Laganá et al. 2010). Atacama Large Millimeter/submillimeter Array (ALMA) observation with 5 arcsec resolution found in RX J1347.5-1145 that $y$ and $S_X$ maps have a single peak, but there is a significant offset between the two peaks (Kitayama et al. 2016). The MUSTANG observation (Mason et al. 2010; Korngut et al. 2011)

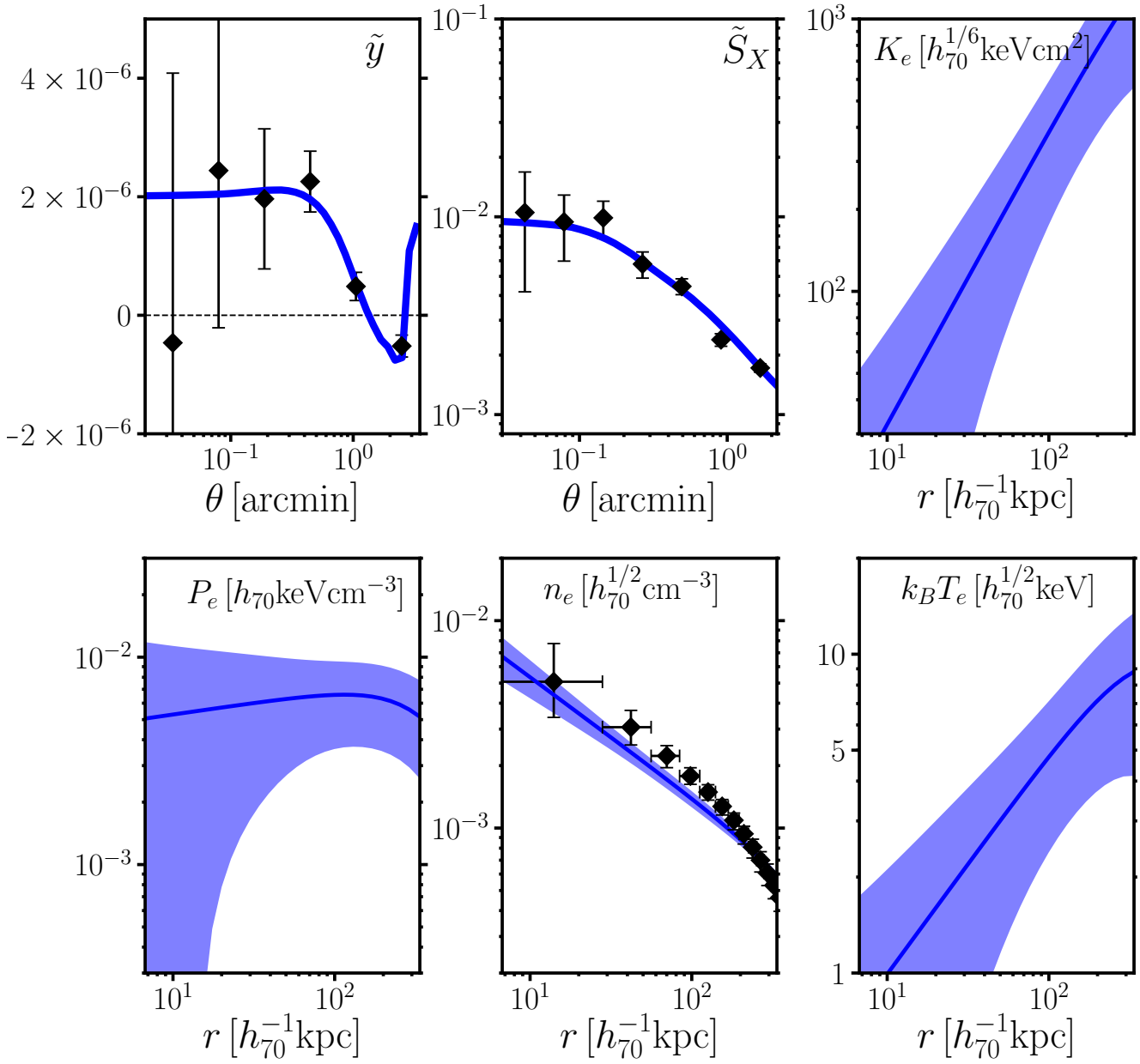


**Figure 14.** The same figure as Figure 3, but for HSC J021056-061154. The signal-to-noise ratios of the $y$ and $S_X$ profiles are $\sim 5\sigma$ and $\sim 16\sigma$, respectively. The increase in the $\tilde{y}_m$ profile at large radii is caused by the transfer function.

shows a negative $y$ parameter around the X-ray peak because of a combination of the offset hot component and the transfer function, which is similar to the result of the minor merger. A residual $y$ pattern is found in the same cluster when fixing the centroid (Plagge et al. 2013; Ueda et al. 2018; Di Mascolo et al. 2019a). However, Di Mascolo et al. (2019a) found no significant residuals from an ellipsoidal pressure profile model with a floating centroid fit.

Kitayama et al. (2004) have measured the temperature of a subcluster in a merging cluster, RX J1347.5-1145 combining the SZE data from Sub-millimeter Common User Bolometer Array (SCUBA) and Nobeyama Bolometer Array (NOBA) and *Chandra* X-ray data and found a hot component with $\sim 20$ keV, for the first time. Their finding of the hot temperature in the merging cluster is similar to those in HSC J023336-053022.

The *Chandra* Observation of the bullet cluster (Markevitch et al. 2002) shows a bow-shock ahead of a stripping cool core and X-ray emission from a main cluster of which the core is elongated along the direction perpendicular to the merger axis. Halverson et al. (2009) detected a SZE signal associated with the main cluster using APEX-SZ with

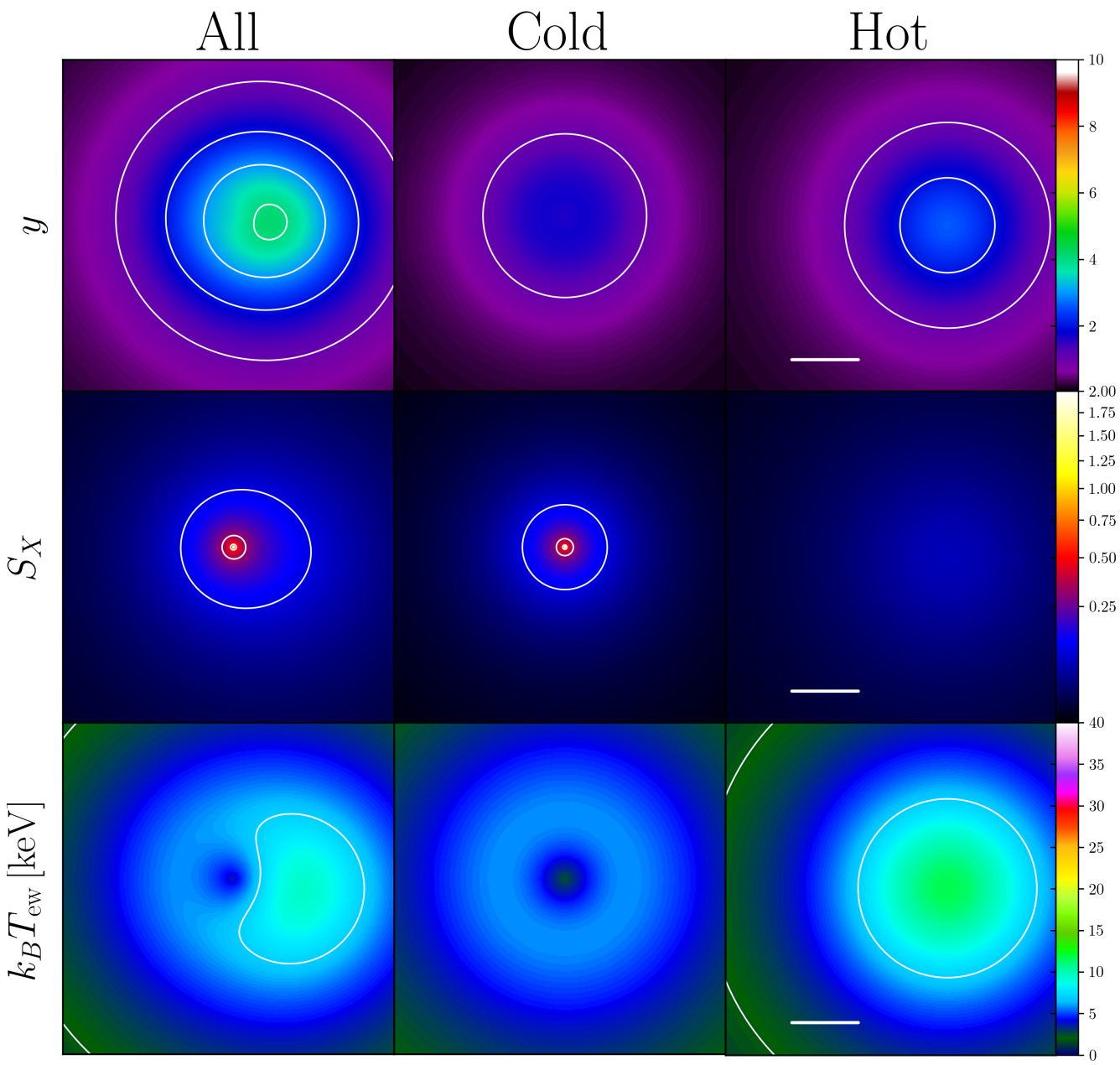


**Figure 15.** Model maps for HSC J021056-061154. Colors, contours and lines are the same as those in Figure 10.

1 arcmin resolution. Di Mascolo et al. (2019b) estimate a Mach number $\mathcal{M} = 2.08 \pm 0.12$ of the bow-shock with ALMA and Atacama Compact (Morita) Array (ACA). However, no high-resolution SZE observation covers the entire region to date.

The Arcminute Microkelvin Imager (AMI; Rumsey et al. 2017) discovered in CIZA J2242.8+5301 an equatorial-shock-heated gas with elongation is perpendicular to both its merger axis and the major axis of the cool core. The relationship of the morphology of $y$ and $S_X$ maps is the same as found in the pre-minor merger, HSC J021056-061154.

Menanteau et al. (2012) found that X-ray and $y$ distribution of the El Gordo cluster is offset similar to the case of RX J1347.5-1145. ALMA observation combined with X-ray data (Basu et al. 2016) constrained a Mach number $\mathcal{M} = 2.4^{+1.3}_{-0.6}$ at an edge of X-ray surface brightness associated with radio relic (Botteon et al. 2016).

Both stacked *Planck* SZE and *RASS* X-ray maps for low-redshift and massive merging clusters (Okabe et al. 2019) found that the $y$ and $S_X$ distributions at cluster outskirts are elongated along the perpendicular direction of the merger axis, though the X-ray main core is elongated along the merger axis.

An offset between X-ray and Compton $y$ parameter dis-

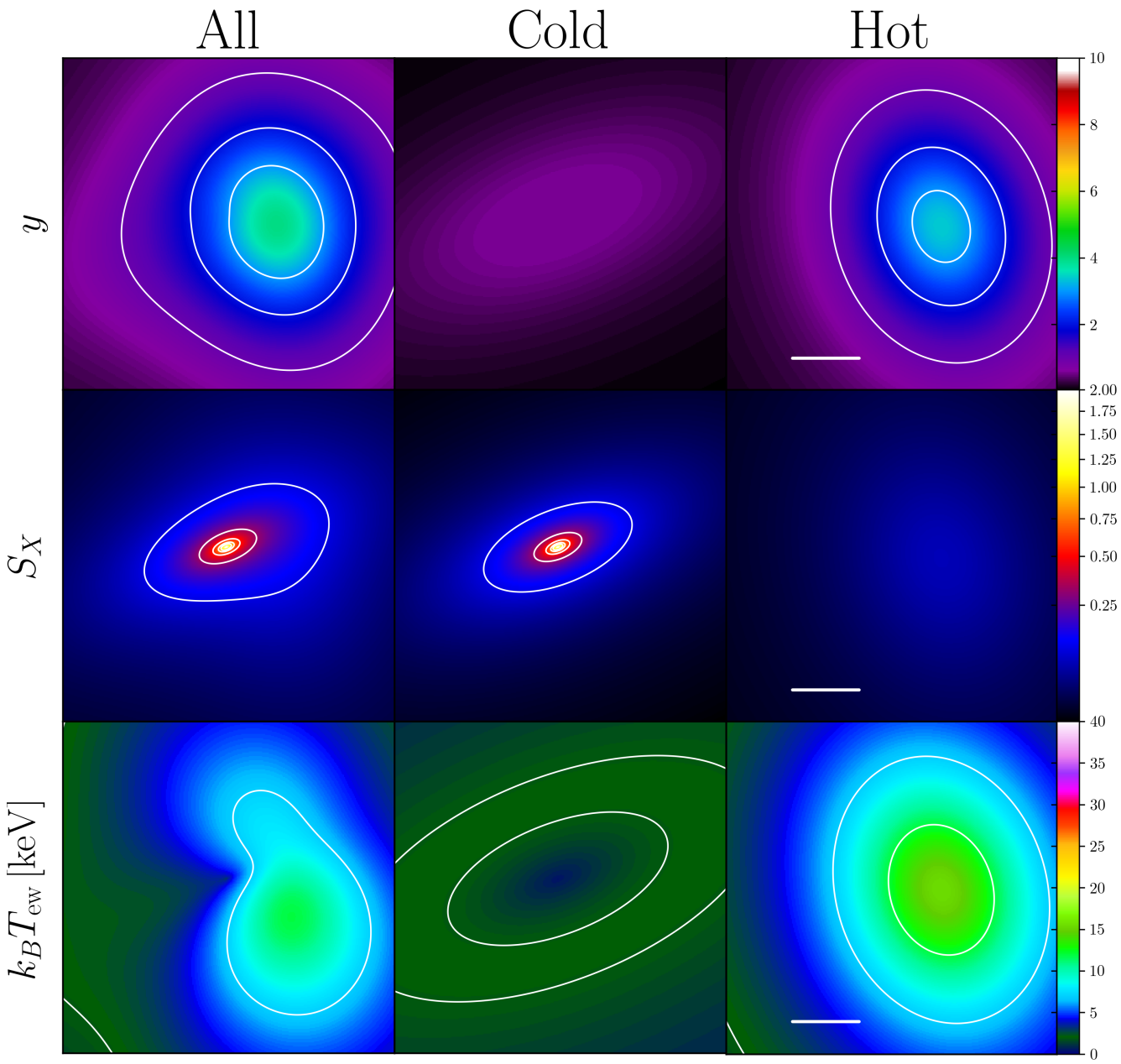


**Figure 16.** Elliptical model maps for HSC J021056-061154. Colors and contours are the same as those in Figure 10.

tributions are commonly found in merging clusters including literature and our sample. A perpendicular orientation angle between the major axes of high $y$ and X-ray core distributions is also found in some clusters. However, the double-peaked $y$ distribution has not yet been reported by observational studies.

### 4.5 Temperature Comparison

We compare the temperatures derived from the joint SZE and X-ray analyses with X-ray temperatures from spectroscopic measurements (Giles et al. 2016; Lieu et al. 2016; Adami et al. 2018). The XXL survey measured the X-ray temperature within $300h_{70}^{-1}$ kpc from the XXL centers. We also use X-ray temperature derived from the deep on-target observation for HSC J022146-034619 from the X-COP measurement (Sec 4.1).

We compute the cylindrical emission-weighted temperatures from our best fits within $300h_{70}^{-1}$ kpc from the XXL centers. Since HSC J023336-053022 and HSC J021056-061154 have complicated $y$ distributions, we use the results of two-dimensional analyses. Figure 18 shows a temperature comparison between from the joint SZE and X-ray analysis, $k_B T_{\rm SZ}$, and the X-ray spectroscopic measurement, $k_B T_{\rm XXL}$.

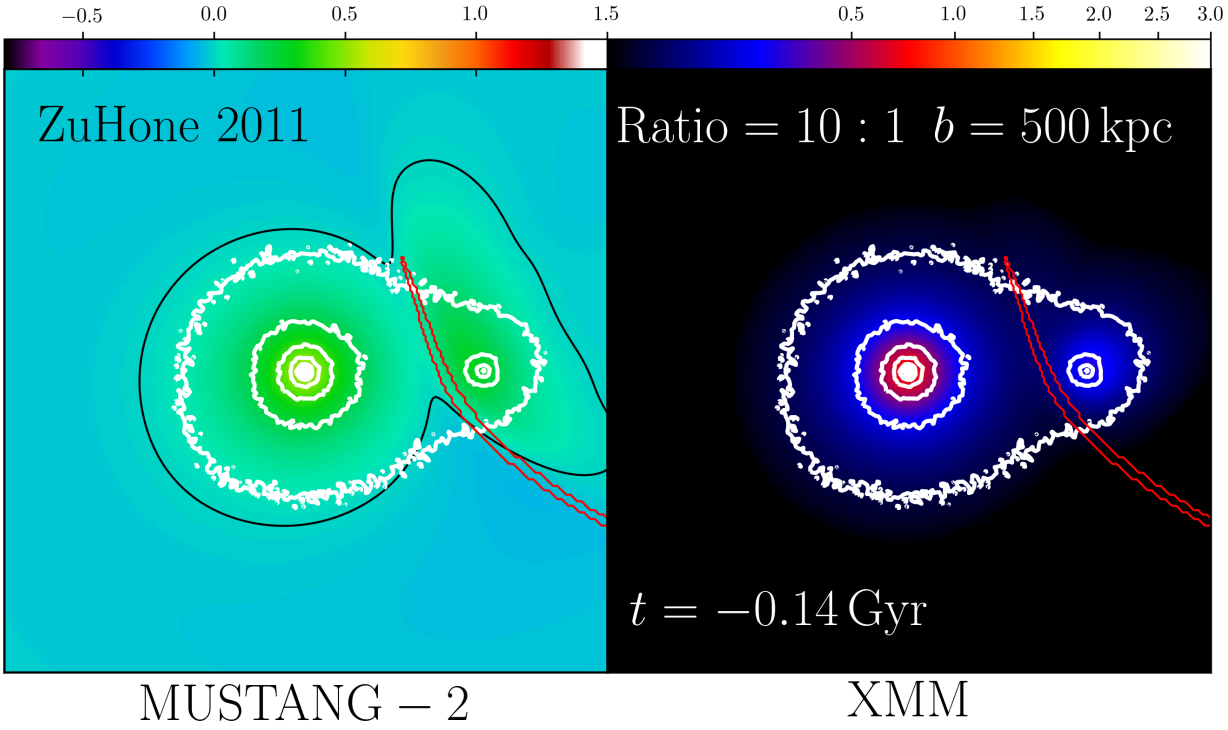


**Figure 17.** Simulated MUSTANG-2 (left) and *XMM-Newton* (right) images (4 arcmin × 4 arcmin) using numerical simulations of ZuHone (2011) publicly available through ZuHone et al. (2018), taking into account the PSFs and the transfer function. The panels are the edge-on view of the merger with 1 : 10 mass ratio and $b = 500$ kpc at 0.14 Gyr before first core-passage, which is a similar case to the minor merger, HSC J021056-061154. Contours are the same as those in Figure 11.

We find in HSC J022146-034619 that the XXL temperature using the XXL survey data and X-COP temperature using the deep pointing observation differ by $\sim 2$ keV which is a $2.3\sigma$ difference, and our result agrees with the latter one. The temperature of the gNFW+$T_{\rm pow}$ model for HSC J022146-034619 does not significantly change from that of the gNFW model. For the three clusters, central projected temperatures derived the joint SZE and X-ray analyses agree well with X-ray temperatures.

Mroczkowski et al. (2009) have found using SunyaevZel'dovich Array (SZA) data that one-dimensional, radial temperature profiles determined from joint SZE and X-ray analysis are in reasonably good agreement with those obtained from an independent X-ray spectroscopic analysis. Romero et al. (2017) have compared SZE temperatures with X-ray temperatures for 14 clusters and found a good agreement $\langle T_{SZ}/T_X \rangle = 1.06 \pm 0.23$ in gas mass weighted temperatures. Although the previous studies did not carry out a multiple component analysis as demonstrated in this paper, our results agree with their results.

### 4.6 Deviations from Scaling Relations

In this section we study whether the dynamical states of the three clusters affect their positions relative to the scaling scaling relations between total mass and temperature ($k_B T_{\rm SZ}$), between total mass and the integrated Compton parameter ($Y_{\rm cyl}$) and between the total and gas mass ($M_{\rm gas}$). We compute gas quantities from the best-fit temperature and density profiles to avoid the PSF smearing effect and the radio transfer function. We use the results of multi-component analyses for HSC J023336-053022 and HSC J021056-061154.

#### *M − T relation*

We first compute emission-weighted temperatures within projected radius $R = 300 h_{70}^{-1}$ kpc from cluster centers following the XXL papers (Lieu et al. 2016). The dashed line in Figure 19 represents the mass–temperature scaling relations composed from the XXL (Pierre et al. 2016), COSMOS (Kettula et al. 2013) and CCCP (Hoekstra et al. 2015) surveys. Umetsu et al. (2019) have carried out weak-lensing analysis using the HSC-SSP 16A shape catalogue and found a slightly lower mass scale than that of Lieu et al. (2016) (the solid line), though they are consistent within $\sim 1\sigma$ errors. The temperature of the single-peaked cluster, HSC J022146-034619, agrees with Lieu et al. (2016). We cannot find significant deviations for the minor merger, HSC J021056-061154, from the best-fit scaling relations, regardless of the models. The temperature for the major merger, HSC J023336-053022, is two or three times higher than implied by the two scaling relations. The temperature of the central cool component still follows the scaling relations. The temperatures of the two hot components are significantly higher than those expected based on their WL masses. These features indicate that the temperature is boosted by the on-going merger (e.g. Ricker & Sarazin 2001). Numerical simulations (e.g. Ricker

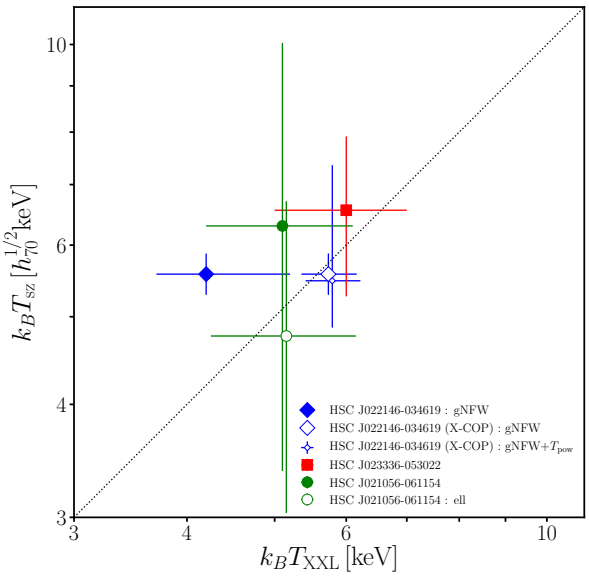


**Figure 18.** Comparison of X-ray and SZE temperatures. Blue diamond, red square, and green circle are HSC J022146-034619, HSC J023336-053022 and HSC J021056-061154, respectively. The open blue diamonds for HSC J022146-034619 denote the X-COP temperature measurement using deep on-source data. The small open diamond is the SZE temperature based on the gNFW+$T_{\rm pow}$ model. The X-ray temperatures of the elliptical model for HSC J021056-061154 (open green circle) and the gNFW+$T_{\rm pow}$ model for HSC J022146-034619 (small open diamond) are shifted by 1.01 for display purposes.

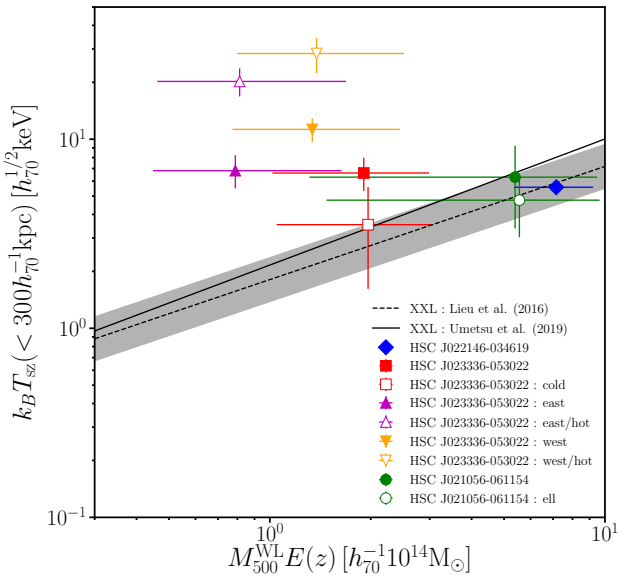


**Figure 19.** Mass-temperature scaling relation at $\Delta = 500$. The emission-weighted temperatures are computed within $300h_{70}^{-1}$ kpc from cluster centers. The solid and dashed lines denote the best-fit scaling relations for the XXL clusters of Umetsu et al. (2019) and Lieu et al. (2016), respectively. The gray region is a combination of the $1\sigma$ uncertainty of the normalization and intrinsic scatter. Blue diamond, red square, orange down-triangle, magenta up-triangle and green circle are HSC J022146-034619, the total, western and eastern component for HSC J023336-053022 and HSC J021056-061154, respectively. The open symbols denote the hot and cold components for the major merger or the elliptical model for the minor merger, respectively. The masses of open symbols are shifted by a factor 1.03 for display purposes. The temperatures of the major merger, HSC J023336-053022, are much higher than those of the scaling relation.

& Sarazin 2001; Poole et al. 2007) for major mergers with mass ratio of 1 : 3 have shown that the temperature increases by a factor of two just after first pericentre passage. Our result is in good agreement with numerical simulations.

### $M - Y_{\rm cyl}$ *relation*

We compute the cylindrical Compton parameter, $Y_{\rm cyl}$ (in units of Mpc$^2$), as follows:

$$Y_{\rm cyl} = 2\pi D_A^2 \int_0^{\theta_{500}} y(\theta')\theta' d\theta' \qquad (19)$$

where $D_A$ is the angular-diameter distance from the observer to the cluster in Mpc, and the enclosed radius, $R_{500} = \theta_{500} D_A$, is determined in the WL analysis[2]. We also propagate errors of the WL-determined $r_{500}$ into the integrated $Y$ parameters. Gupta et al. (2017) found that a conversion factor from a spherical integrated $Y$ parameter to a cylindrical Y parameter is 1.151. We convert from a spherical $Y$ parameter using a numerical simulation (Yu et al. 2015) to the cylindrical $Y$ parameter which is shown by the solid line in Figure 20. The normalizations of two numerical simulations (Yu et al. 2015; Gupta et al. 2017) agree well with each other. The $Y$ parameter of the single-peaked cluster, HSC J022146-034619, is half the expected value given its mass. This is caused by the normalization of the electron pressure profile being lower than expected from the *Planck* SZE pressure profile (Planck Collaboration et al. 2013). The minor merger agrees with the numerical simulations. Since the model pressure outside the core of the minor merger is higher than those of the other clusters, the integrated $Y$ of this cluster is comparable though its peak signal-to-noise ratio is lower. However, the $Y$ parameters of the major merger are about ten times higher than the scaling relation suggests. Poole et al. (2007) have investigated using numerical simulations the time evolution of the cylindrical Compton $Y$ parameter within $R_{2500}$ and found that it increases by about a factor four just after first pericentre of major merger with 1:3 mass ratio. Wik et al. (2008) have shown that the simulated spherical Compton $Y$ parameter over the entire region of clusters increases by about 50 percent times in major mergers with 1:3 mass ratio. Although the measurement methods are different, the increase in the $Y$ parameter provides similar trends to our results. However, Yu et al. (2015) have shown in numerical simulations that

[2] We note that arcmin$^2$ and steradians are other common units for $Y$ used in the literature, in which case the $D_A^2$ factor should be omitted from Equation(19) and corresponding units of angles or solid angles should be used in the integral.

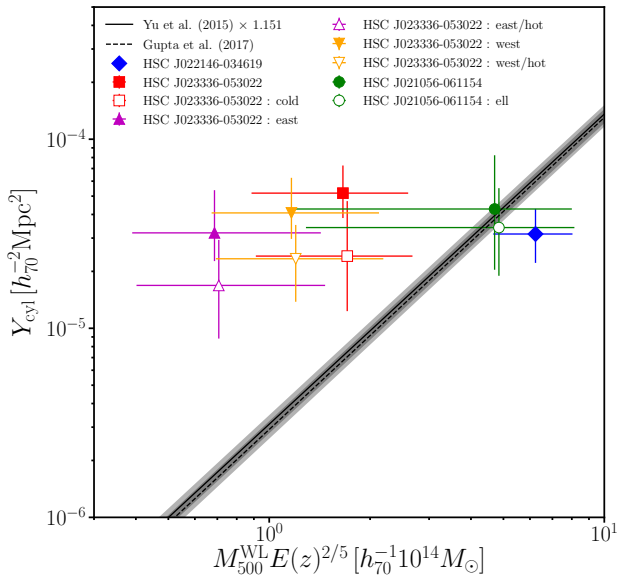


**Figure 20.** Scaling relation of the WL mass and cylindrical $Y$ parameter at $\Delta = 500$. The solid and dashed lines denote the best-fit scaling relations from the numerical simulations of Yu et al. (2015) and Gupta et al. (2017), respectively. Colour symbols and gray region are the same as Figure 19. The $Y$ parameters of the major merger significantly depart from the scaling relation.

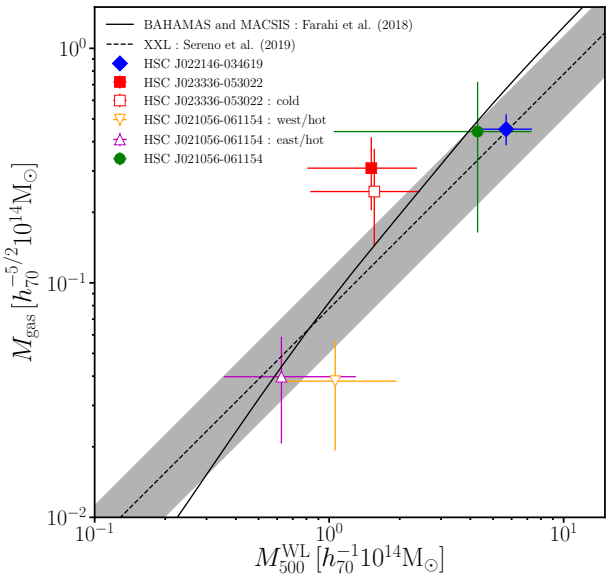


**Figure 21.** Relation between the WL mass and gas mass within spherical radius, $r_{500}$. The solid and dashed lines denote the best-fit scaling relations from numerical simulations (Farahi et al. 2018) and the XXL clusters (Sereno et al. 2019), respectively. Colour symbols and gray region are the same as Figure 19.

the spherical $Y$ parameter of the thermal component has no significant merger boost at 0.15 Gyr after core passage and that the scatter of the $Y$ parameter in the scaling relation is at most about 20 per cent. This is not supported by our data.

### *$M - M_{\rm gas}$ relation*

We also investigate the relation between total mass, inferred from WL analysis, and gas mass within each cluster's spherical radius $r_{500}$, as shown in Figure 21. The cases of the major and minor mergers use the results of the multi-component analyses. In three-dimensional dimensions we calculate the off-centering effect of each component, as follows

$$\rho^{\rm off}(r) = \frac{1}{2\pi^2}\int_0^\pi d\theta \int_0^{2\pi} d\phi \, \rho(\sqrt{d_{\rm off}^2 + r^2 - 2rd_{\rm off}\cos\theta\sin\phi}), \quad (20)$$

where $\rho$ is the mass density, $d_{\rm off}$ is the off-centering radius and $r$ is the distance from the center in the three-dimensional space. We ignore the separation between components along the line of sight. Since the central component dominates for the gas mass, this assumption does not significantly change the result. We propagate errors of the WL-determined $r_{500}$ into gas mass estimates. We also plot a theoretical scaling relation from cosmological hydrodynamical simulations (Farahi et al. 2018) and the scaling relation (Sereno et al. 2019) derived for the XXL sample (assuming $M_{\rm gas} \propto M$ and no evolution) based on the HSC-WL (Umetsu et al. 2019) and XXL survey data. We find that the total gas mass within the major merger (red square) and the gas mass for the western hot component of the major merger (orange triangle) are slightly higher and lower than the baseline scaling relations, respectively. If the gas mass follows the scaling relations before the merger, the feature suggests a possibility that a small fraction of the gas mass of the main cluster is moved to the region of the subcluster. Indeed, the X-ray core is composed of the two components (Sec 4.1). The surface-brightess weighted center close to the secondary X-ray peak is at the intermediate position of the two $y$ peaks and the main X-ray peak is close to the eastern component. Some fraction of the X-ray core could be a remnant of the main cluster.

### *Time evolution*

We investigate how much the temperature and the integrated Compton $y$ parameter change with dynamical time during cluster mergers, as discussed above. Assuming that the gas properties before cluster mergers follow the scaling relations (Lieu et al. 2016; Gupta et al. 2017), we compute the ratio between the observable and the expectation of WL masses via the scaling relations, $f(M)$ . The range of plausible dynamical times is estimated by spatial separations between WL-determined centres (Sec. 4.2) or galaxy clumps (Secs. 4.1 and 4.3) and inferred velocity. The dynamical time is normalized by the sound-crossing time to allow comparisons from different mass systems. We ignore the distance along the line of sight. We assume that the dynamical time ranges are 0.1 Gyr for the pre- and post mergers and 1 Gyr for the sloshing phase as uncertainties. The result is shown in Figure 22. The errors in the scaled $Y_{\rm SZ}$ and $k_BT$ values for each cluster take into account the

$1\sigma$ uncertainties of both spherically symmetric gas models and WL masses. We also plot results of N-body and hydrodynamic numerical simulations of binary mergers (ZuHone 2011) and sloshing (ZuHone et al. 2010) which are computed from the publically-available catalogue (ZuHone et al. 2018). The solid, dashed and dotted lines are the time evolution for head-on mergers of mass ratio 1 : 1, 1 : 3 and 1 : 10 from ZuHone (2011), respectively. The dash-dotted line is for mass ratio of 1 : 20 with impact parameter of 200 kpc, retrieved from ZuHone et al. (2010). The first two and last one are references for the major and minor mergers, respectively. We normalized the simulated gas properties by the initial states. The temperature and the integrated Compton $y$ parameter of ZuHone (2011) are as would be observed for a merger in the plane of the sky, and calculated within 300 kpc for the temperature and $r_{500}$ for the integrated Compton $y$ parameter from X-ray surface brightness peaks. The off-axis merger of the sloshing simulation (ZuHone et al. 2010) are calculated for the same direction as Figure 8. The overall trend of the time evolution from numerical simulations do not conflict with our results. Although the current sample of clusters is only three, future follow-up studies will significantly increase the number of clusters. A large sample of merging clusters (Okabe et al. 2019) will fill the parameter space of the dynamical time and the mass ratio, and statistically overcome uncertainties in the values of the impact parameter of cluster mergers, inclination angle of cluster mergers relative to the plane of sky, and intrinsic scatter of initial states.

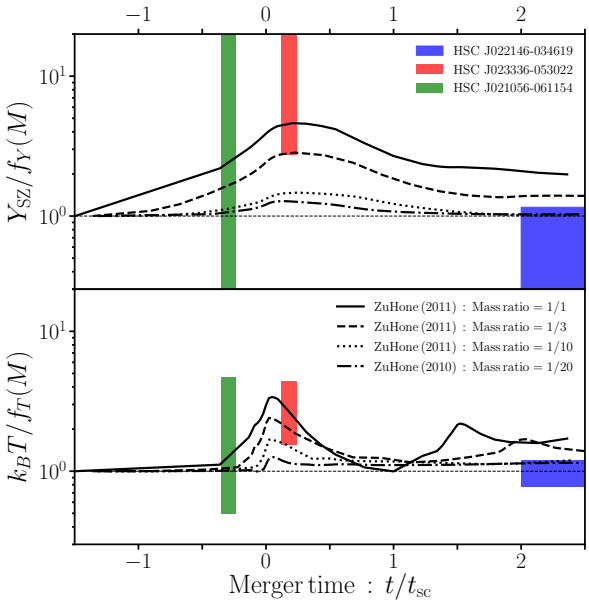


**Figure 22.** Time evolution of the merger boost. The $x$-axis is the time in units of the sound-crossing time. The function, $f(M)$, is the temperature or the integrated Compton $y$ parameter expected from the WL masses on the basis of the scaling relations (Lieu et al. 2016; Gupta et al. 2017). From left to right, rectangles mark HSC J021056-061154, HSC J023336-053022, and HSC J022146-034619, respectively. The errors in $y$-axes take into account the $1\sigma$ uncertainties of both gas measurements and WL masses. The solid, dashed and dotted lines are results of numerical simulations (ZuHone 2011) of mass ratio 1 : 1, 1 : 3 and 1 : 10 respectively, assuming head-on mergers. The dash-dotted line shows the result of numerical simulations (ZuHone et al. 2010) of mass ratio 1 : 20 with an impact parameter of 200 kpc.

### 4.7 Central entropy index profiles and centroid offsets

The distribution of galaxies provides a strong indication of whether a cluster is undergoing a major merger, and the phase of that interaction, but cannot inform us about the status of the cluster atmospheres. Further, optical searches are not good at identifying low-mass subhalos and mergers where the halo barycentres are closely spaced. Since gas properties are more or less changed by both major and minor mergers, and the duration of the change continues over several sound-crossing times (e.g. Ricker & Sarazin 2001; Poole et al. 2007; Wik et al. 2008; ZuHone 2011), and repeated interactions with small subhalos can sustain X-ray perturbation (Ascasibar & Markevitch 2006; ZuHone et al. 2010), the gas properties provides us with the essential information of the activity of gas, which is complementary to the optical galaxy distributions.

Pratt et al. (2010) have investigated cluster dynamical properties using X-ray based entropy index profiles in the inner regions of 31 nearby clusters ($z \lesssim 0.15$) from the representative XMM-Newton cluster structure survey (REXCESS). They assumed a spherically symmetric model and found that the central entropy for morphologically disturbed clusters is higher than the baseline expected from cosmological simulations (Voit et al. 2005), but that for cool core clusters follows the baseline. That feature would be explained by the scenario that merging subhalos penetrate into central regions of the main clusters, and then heat and disturb the central gas. We therefore investigate central entropy profiles. Following Pratt et al. (2010), we first assume a spherically-symmetric model from one-dimensional analysis. We normalized the radius by the WL-determined $r_{500}$ and the entropy by the characteristic entropy computed by WL masses. The characteristic entropy is specified by eq. (3) of Pratt et al. (2010). We here ignore WL measurement errors for simplicity. The resulting profiles of electron entropy index are higher than the baseline from numerical simulations (Voit et al. 2005), as shown in the left panel of Figure 23. The electron entropy index at $r \sim 0.01 r_{500}$ is $\sim 0.1 K_{500}$, which is similar to the case of the morphologically disturbed clusters of Pratt et al. (2010). Indeed, the $y$ and $S_X$ maps for the three clusters are complexly distributed. Since we have carried out multi-component analyses, we computed the corresponding profiles for the main cluster component of the gNFW model. The right panel of Figure 23 shows that the entropy for the main cluster component follows the baseline. That suggests that, when we interpret the entropy profile in the three dimensional space from the projected information, the geometrical assumption and the number of components are both important. If the hot component is located offset from the cluster center, the entropy index close to the centre for the spherical model would be overestimated due to the low-density in this region.

We next compare centroids determined by the two-dimensional analyses (Table 4 ) with the BCG positions. The left and right panels in Figure 24 show gas center and

mass center offsets. The gas centers are obtained by a forward modeling method, and thus differ from the peak positions of the SZE and/or X-ray distributions. The mass center for the pre-minor merger, HSC J021056-061154, cannot be estimated since there is no shape catalogue in the central region (Sec. 3.4). The gas offsets for the sloshing cluster, HSC J022146-034619 and the pre-minor merger are smaller than those of the major-merger, HSC J023336-053022. We adopted the single gNFW model for HSC J022146-034619. The WL-determined centroids for the major merger agree with the BCGs (Sec. 4.2.2), while that for the sloshing cluster is slightly offset (Sec. 4.1.2). Offset features in gas and mass distributions show different trends and have no correlation with central entropy profiles. Therefore, the offset distances, especially gas centers, will give complementary indicators about the dynamical state.

### 4.8 Mass Comparison

We compare hydrostatic equilibrium (HE) masses with weak-lensing (WL) masses as a function of radius. The HE masses are evaluated through the HE equation

$$M_{\rm HE}(<r) = -\frac{r^2}{G\mu m_p n_e}\frac{dP_e}{dr} \quad (21)$$

where $\mu = 0.62$ is the mean molecular weight. For the multi-component gas analysis, we take account of the off-centering effect (eq. 20) for the electron number density and pressure profiles but ignore the offsets along the line of sight. Similarly, the two WL mass estimates by the two-dimensional analysis are converted into one-dimensional radial profiles through the off-centering effect in the mass density. Figure 25 shows the spherical mass profiles derived by the joint SZE and X-ray analysis and by WL analysis. The figure also shows the mass ratio $M_{\rm HE}/M_{\rm WL}$ out to $300\,h_{70}^{-1}$kpc which is comparable to the maximum radii ($\sim$ 1 arcmin) of our positive $y$ measurements. Since we cannot use a shape catalogue in the central region, the WL measurement errors for HSC J021056-061154 are large and the mass ratio cannot be constrained well. We find for the single-peaked cluster, HSC J022146-034619, that the HE mass is consistent with the WL one, while for the merging cluster, HSC J023336-053022, that the HE mass exceeds the WL one because of the merger-boost.

Although it is difficult to make a fair comparison with the literature because of the small set of clusters and a difference of radial range, agreement of the HE and WL mass estimations of $M_{500}$ are also reported by Local Cluster Substructure Survey (LoCuSS; Smith et al. 2016) and the XXL Survey (Sereno et al. 2019).

## 5 CONCLUSIONS

We performed GBT/MUSTANG-2 observations for three HSC-SSP CAMIRA clusters (Oguri et al. 2018) with different galaxy distributions: one single-peaked cluster; one double-peaked cluster; and a part of supercluster.

We compared the $y$ maps with X-ray images taken from the XXL survey and HSC optical galaxy distributions. The gas distributions observed by the SZE and X-ray method give us different information. The single-peaked cluster, HSC J022146-034619, exhibits SZE and X-ray distributions with regular morphology and an elongated galaxy distribution. The residual $y$ and $S_X$ patterns from the azimuthally averaged profiles are coherent, indicating that the cluster is in a sloshing phase. The double-peaked cluster, HSC J023336-053022, shows a double-peaked $y$ morphology with each peak associated with a separate galaxy concentration and a single X-ray core between the two $y$ peaks. Such a double-peaked $y$ feature is not yet reported in previous studies. The cluster is likely to be a major merger just after core-passage. The supercluster component, HSC J021056-061154, shows an elongated $y$ distribution offset from the X-ray main peak around the BCG position, indicating a pre-minor merger. The gas properties (temperature, density and pressure) are more or less disturbed regardless of the global red galaxy distributions.

We performed Bayesian forward modeling via simultaneous fits to MUSTANG-2 $y$ and XXL X-ray data and measure gas properties. The multi-component analysis of the major-merger system revealed two hot regions with temperatures of $\sim 20-30$ keV and a cool core component. The minor merger has a hot component elongated perpendicular to the major-axis of the X-ray core. Combined with WL mass or stellar mass estimates, the major and minor mergers are likely to be seen after core crossing with mass ratio $\sim 2:3$ and pre-merger with ratio $\sim 1:10$, respectively. As for the single-peaked cluster, there are two subhalo candidates which plausibly drive the sloshing mode. The overall features of the merger geometry and gas quantities agree with predictions from numerical simulations (ZuHone 2011).

We did not find significant levels of diffuse radio emission in the FIRST, GMRT and TGSS data with high angular resolutions. The absence of diffuse radio emission implies an efficiency of less than 1 percent for conversion of kinetic energy into relativistic electrons, assuming a magnetic field strength $B > 1\,\mu$G.

We studied deviations from the mass scaling relations of the temperature, the integrated $Y_{\rm cyl}$ parameter, and the gas mass and a relationship with their dynamical dependence. We found a significant merger-driven boost in the M-T and $Y_{\rm cyl}$ relations and good agreement with numerical simulations (ZuHone 2011). Although the $y$ and $S_X$ distributions of all the three clusters are disturbed, the global $k_BT$ and $Y_{\rm cyl}$ are significantly changed only for the major merger just after core-passage.

The joint analysis of the high-angular resolution SZE and X-ray data enables us to simultaneously determine the three-dimensional profiles of the temperature and the density and their centers. It can spatially resolve hot components at temperatures of tens of keV which are not well measured by existing X-ray satellites. The spatial resolution of the projected temperature distribution is $\sim 0.05\,{\rm arcmin}^2$ and higher than those of X-ray spectroscopic measurement (the order of the ${\rm arcmin}^2$). Therefore, such analyses can overcome the problems of poor angular resolution of X-ray temperature measurements and provide a tool for studying the hottest components of clusters and cluster mergers. In the future, systematic follow-up observations for optical clusters in various dynamical stages will play an important role in cluster physics.

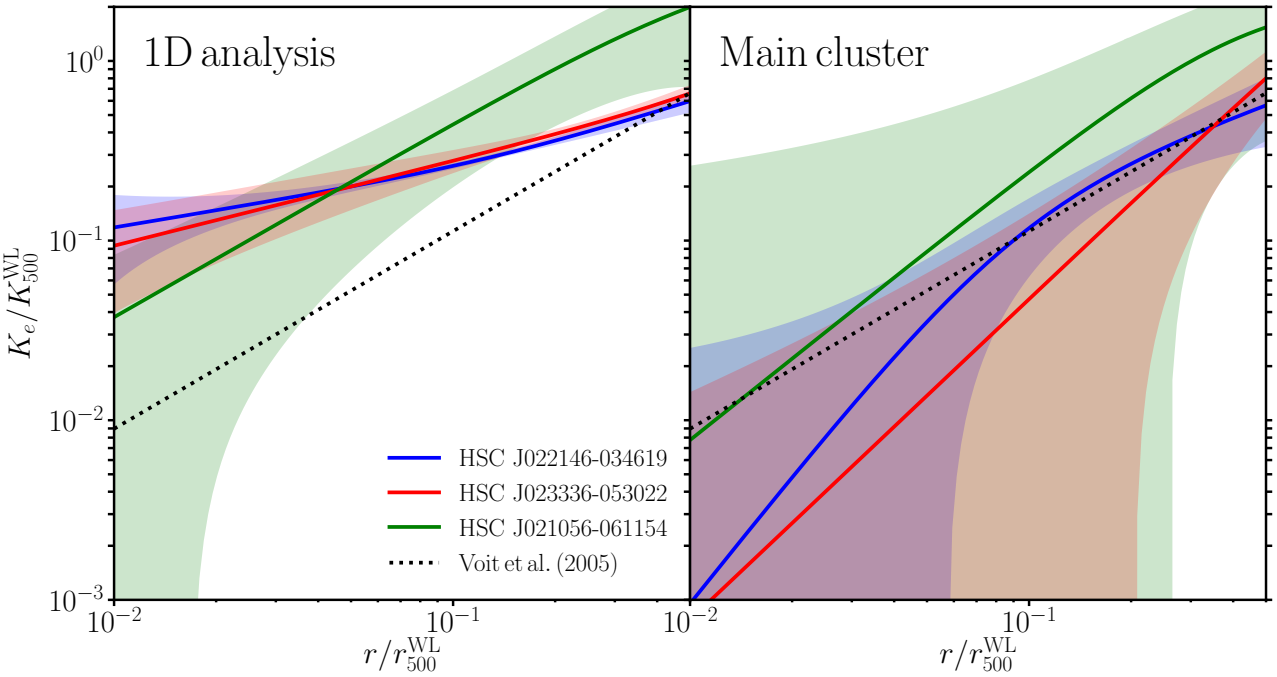


**Figure 23.** Central entropy index profiles normalized by weak-lensing radii and masses. *Left:* results from one-dimensional analysis. *Right*: results for the main cluster components (gNFW model) derived from the multicomponent analysis. Blue, red and green solid lines are HSC J022146-034619, HSC J023336-053022 and HSC J021056-061154, respectively. The colour shaded regions represent the $1\sigma$ uncertainty bounds. The black dotted line is $K/K_{500} = 1.41(r/r_{500})^{1.1}$ of Voit et al. (2005). $K_{500} = 375\mathrm{keV\,cm^2}\left(M_{500}^{\rm WL}/10^{14}h_{70}^{-1}M_\odot E(z)\right)^{2/3}(f_b/0.15)^{-2/3}$ from eq (3) of Pratt et al. (2010), where $f_b$ is the baryon fraction.

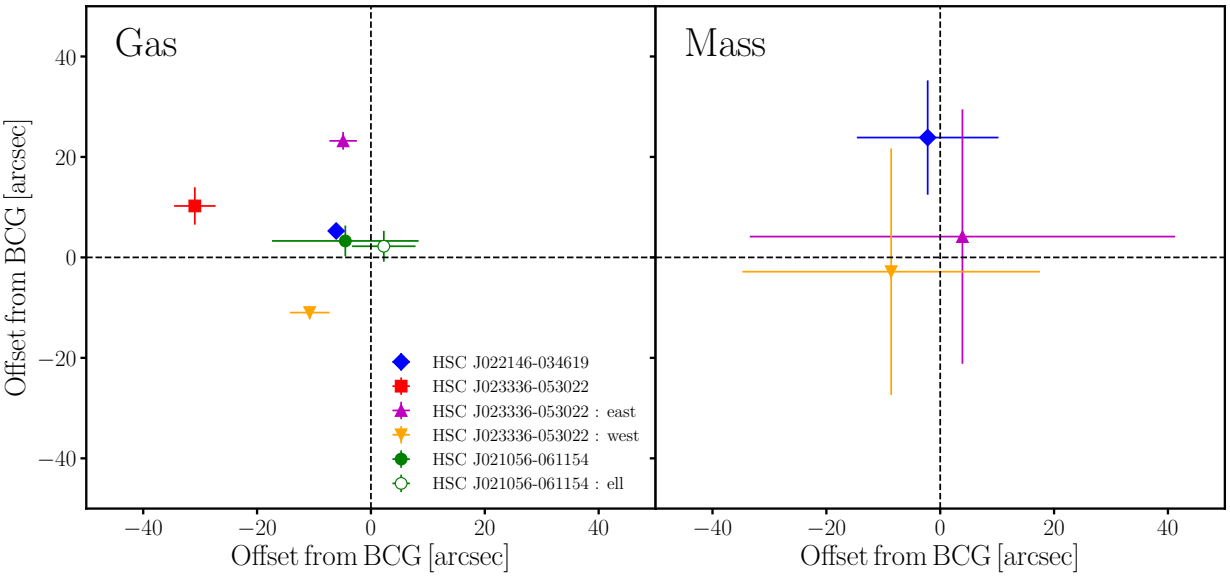


**Figure 24.** *Left*: offsets between gas centers obtained by the two-dimensional joint SZE and X-ray analysis and the BCGs. *Right* offsets between mass centers determined by the two-dimensional analysis and the BCGs. Colour symbols are the same as Figure 19.

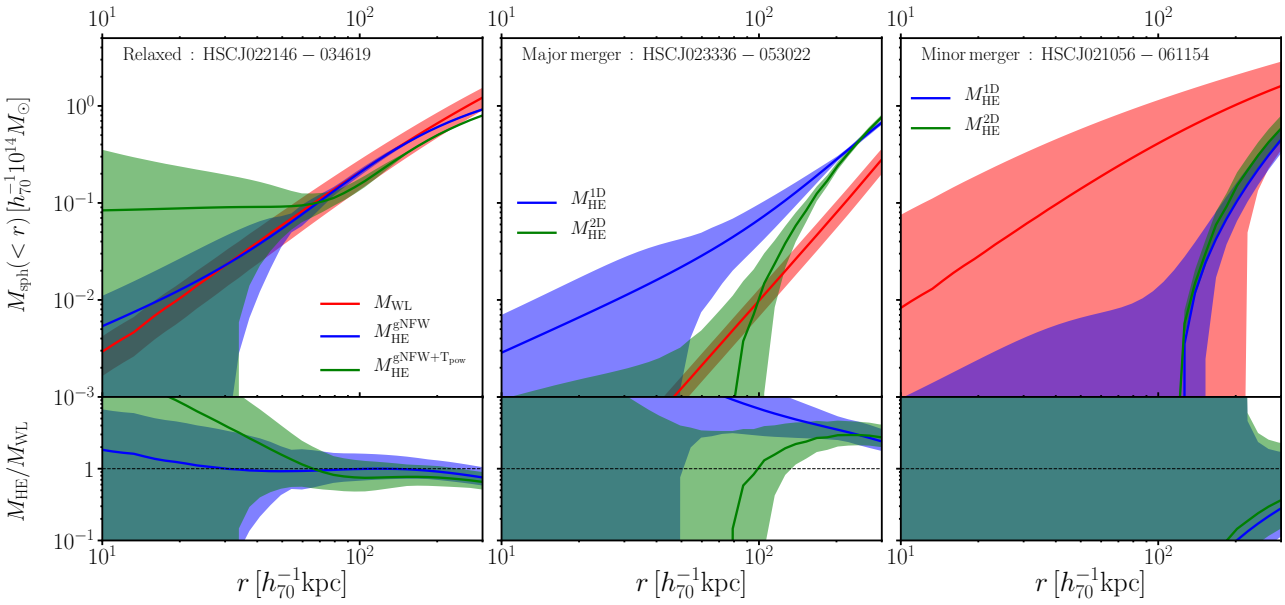


**Figure 25.** *Top*: HE and WL enclosed masses as a function of 3-D radius (from left to right ; HSC J022146-034619, HSC J023336-053022 and HSC J021056-061154) . The red and blue lines denote the WL and HE mass profiles, respectively. The green lines are the HE mass profile derived from gNFW+$T_{\rm pow}$ model in the left panel and two-dimensional analysis in the middle and right panels. The color transparent regions denote the $1\sigma$ uncertainty. *Bottom*: HE to WL total mass ratios as a function of radius.

## ACKNOWLEDGMENTS

MUSTANG2 is supported by the NSF award number 1615604 and by the Mt. Cuba Astronomical Foundation. The National Radio Astronomy Observatory is a facility of the National Science Foundation operated under cooperative agreement by Associated Universities, Inc. GBT data was taken under the project ID AGBT17B_101.

The Hyper Suprime-Cam (HSC) collaboration includes the astronomical communities of Japan and Taiwan, and Princeton University. The HSC instrumentation and software were developed by the National Astronomical Observatory of Japan (NAOJ), the Kavli Institute for the Physics and Mathematics of the Universe (Kavli IPMU), the University of Tokyo, the High Energy Accelerator Research Organization (KEK), the Academia Sinica Institute for Astronomy and Astrophysics in Taiwan (ASIAA), and Princeton University. Funding was contributed by the FIRST program from Japanese Cabinet Office, the Ministry of Education, Culture, Sports, Science and Technology (MEXT), the Japan Society for the Promotion of Science (JSPS), Japan Science and Technology Agency (JST), the Toray Science Foundation, NAOJ, Kavli IPMU, KEK, ASIAA, and Princeton University.

This paper makes use of software developed for the Large Synoptic Survey Telescope. We thank the LSST Project for making their code available as free software at `http://dm.lsst.org`.

The Pan-STARRS1 Surveys (PS1) have been made possible through contributions of the Institute for Astronomy, the University of Hawaii, the Pan-STARRS Project Office, the Max-Planck Society and its participating institutes, the Max Planck Institute for Astronomy, Heidelberg and the Max Planck Institute for Extraterrestrial Physics, Garching, The Johns Hopkins University, Durham University, the University of Edinburgh, Queens University Belfast, the Harvard-Smithsonian Center for Astrophysics, the Las Cumbres Observatory Global Telescope Network Incorporated, the National Central University of Taiwan, the Space Telescope Science Institute, the National Aeronautics and Space Administration under Grant No. NNX08AR22G issued through the Planetary Science Division of the NASA Science Mission Directorate, the National Science Foundation under Grant No. AST-1238877, the University of Maryland, and Eotvos Lorand University (ELTE) and the Los Alamos National Laboratory.

Based on data collected at the Subaru Telescope and retrieved from the HSC data archive system, which is operated by Subaru Telescope and Astronomy Data Center at National Astronomical Observatory of Japan.

XXL is an international project based around an XMM Very Large Programme surveying two 25 deg$^2$ extragalactic fields at a depth of $\sim 6\times10^{-15}\,{\rm erg\,cm^{-2}\,s^{-1}}$ in the [0.5-2] keV band for point-like sources. The XXL website is http://irfu.cea.fr/xxl. Multi-band information and spectroscopic follow-up of the X-ray sources are obtained through a number of survey programmes, summarised at http://xxlmultiwave.pbworks.com/.

This work was in part supported by the Funds for the Development of Human Resources in Science and Technology under MEXT, Japan and Core Research for Energetic Universe in Hiroshima University and in-house grant for international conferences under the MEXT's Program for Promoting the Enhancement of Research Universities, Japan.

This paper is supported in part by JSPS KAKENHI Grant Number JP18K03704 (T. K.), JP15H05892 (M.O.) and JP18K03693 (M. O.) . SRON is supported financially by NWO, the Netherlands Organization for Scientific Research.

KU acknowledges support from the Ministry of Science and Technology of Taiwan (grant MOST 106-2628-M-001-003-MY3) and from the Academia Sinica Investigator Award (grant AS-IA-107-M01).

We acknowledge Lucio Chiappetti for his editorial comments on the manuscript.

## REFERENCES

Adami C., et al., 2018, A&A, 620, A5
Aihara H., et al., 2018a, PASJ, 70, S4
Aihara H., et al., 2018b, PASJ, 70, S8
Aihara H., et al., 2019, arXiv:1905.12221, p. arXiv:1905.12221
Arnaud M., Pratt G. W., Piffaretti R., Böhringer H., Croston J. H., Pointecouteau E., 2010, A&A, 517, A92
Ascasibar Y., Markevitch M., 2006, ApJ, 650, 102
Basu K., Sommer M., Erler J., Eckert D., Vazza F., Magnelli B., Bertoldi F., Tozzi P., 2016, The Astrophysical Journal, 829, L23
Birkinshaw M., 1999, Phys. Rep., 310, 97
Bleem L. E., et al., 2015, ApJS, 216, 27
Böhringer H., et al., 2004, A&A, 425, 367
Bosch J., et al., 2018, PASJ, 70, S5
Botteon A., Gastaldello F., Brunetti G., Kale R., 2016, MNRAS, 463, 1534
Botteon A., Brunetti G., Ryu D., Roh S., 2019, arXiv e-prints, p. arXiv:1907.00966
Bouillot V. R., Alimi J.-M., Corasaniti P.-S., Rasera Y., 2015, MNRAS, 450, 145
Bradač M., et al., 2006, ApJ, 652, 937
Carrasco Kind M., Brunner R. J., 2014, MNRAS, 438, 3409
Cassano R., et al., 2013, ApJ, 777, 141
Cavaliere A., Fusco-Femiano R., 1976, A&A, 500, 95
Condon J. J., Cotton W. D., Greisen E. W., Yin Q. F., Perley R. A., Taylor G. B., Broderick J. J., 1998, AJ, 115, 1693
Coupon J., Czakon N., Bosch J., Komiyama Y., Medezinski E., Miyazaki S., Oguri M., 2018, PASJ, 70, S7
Di Mascolo L., Churazov E., Mroczkowski T., 2019a, MNRAS, 487, 4037
Di Mascolo L., et al., 2019b, Astronomy and Astrophysics, 628, A100
Dicker S. R., et al., 2014, Journal of Low Temperature Physics, 176, 808
Diemer B., Kravtsov A. V., 2015, ApJ, 799, 108
Drury L. O., 1983, Reports on Progress in Physics, 46, 973
Eckert D., Molendi S., Paltani S., 2011, A&A, 526, A79
Eckert D., Ettori S., Pointecouteau E., Molendi S., Paltani S., Tchernin C., 2017, Astronomische Nachrichten, 338, 293
Eckert D., et al., 2019, A&A, 621, A40
Ettori S., Donnarumma A., Pointecouteau E., Reiprich T. H., Giodini S., Lovisari L., Schmidt R. W., 2013, Space Science Reviews, 177, 119
Ettori S., et al., 2019, A&A, 621, A39
Farahi A., Evrard A. E., McCarthy I., Barnes D. J., Kay S. T., 2018, MNRAS, 478, 2618
Furusawa H., et al., 2018, PASJ, 70, S3
Ghirardini V., Ettori S., Eckert D., Molendi S., Gastaldello F., Pointecouteau E., Hurier G., Bourdin H., 2018, A&A, 614, A7
Giles P. A., et al., 2016, A&A, 592, A3
Gralla M. B., et al., 2014, MNRAS, 445, 460
Guglielmo V., et al., 2018, A&A, 620, A7
Gupta N., Saro A., Mohr J. J., Dolag K., Liu J., 2017, MNRAS, 469, 3069
Ha J.-H., Ryu D., Kang H., 2018, ApJ, 857, 26
Halverson N. W., et al., 2009, The Astrophysical Journal, 701, 42
Helfand D. J., White R. L., Becker R. H., 2015, ApJ, 801, 26
Hirata C., Seljak U., 2003, MNRAS, 343, 459
Hlavacek-Larrondo J., et al., 2018, MNRAS, 475, 2743
Hoekstra H., Herbonnet R., Muzzin A., Babul A., Mahdavi A., Viola M., Cacciato M., 2015, MNRAS, 449, 685
Huang S., et al., 2018, PASJ, 70, S6
Hughes J. P., Birkinshaw M., 1998, ApJ, 501, 1
Ichikawa K., et al., 2013, ApJ, 766, 90
Intema H. T., Jagannathan P., Mooley K. P., Frail D. A., 2017, A&A, 598, A78
Kang H., Ryu D., 2013, ApJ, 764, 95
Kawanomoto S., et al., 2018, PASJ, 70, 66
Kettula K., et al., 2013, ApJ, 778, 74
King L. J., et al., 2016, MNRAS, 459, 517
Kitayama T., Komatsu E., Ota N., Kuwabara T., Suto Y., Yoshikawa K., Hattori M., Matsuo H., 2004, PASJ, 56, 17
Kitayama T., et al., 2016, Publications of the Astronomical Society of Japan, 68, 88
Komiyama Y., et al., 2018, ApJ, 853, 29
Korngut P. M., et al., 2011, ApJ, 734, 10
Laganá T. F., Andrade-Santos F., Lima Neto G. B., 2010, A&A, 511, A15
Lieu M., et al., 2016, A&A, 592, A4
Mandelbaum R., et al., 2018a, PASJ, 70, S25
Mandelbaum R., et al., 2018b, MNRAS, 481, 3170
Markevitch M., Gonzalez A. H., David L., Vikhlinin A., Murray S., Forman W., Jones C., Tucker W., 2002, The Astrophysical Journal, 567, L27
Mason B. S., et al., 2010, The Astrophysical Journal, 716, 739
Medezinski E., Umetsu K., Okabe N., Nonino M., Molnar S., Massey R., Dupke R., Merten J., 2016, The Astrophysical Journal, 817, 24
Medezinski E., et al., 2018a, PASJ, 70, 30
Medezinski E., et al., 2018b, PASJ, 70, S28
Menanteau F., et al., 2012, The Astrophysical Journal, 748, 7
Miniati F., Jones T. W., Kang H., Ryu D., 2001, ApJ, 562, 233
Miyaoka K., et al., 2018, PASJ, 70, S22
Miyatake H., et al., 2019, ApJ, 875, 63
Miyazaki S., Hamana T., Ellis R. S., Kashikawa N., Massey R. J., Taylor J., Refregier A., 2007, ApJ, 669, 714
Miyazaki S., et al., 2018a, PASJ, 70, S1
Miyazaki S., et al., 2018b, PASJ, 70, S27
Mroczkowski T., et al., 2009, The Astrophysical Journal, 694, 1034
Mroczkowski T., et al., 2019, Space Sci. Rev., 215, 17
Murata R., et al., 2019, ArXiv, p. arXiv:1904.07524
Nagai D., Vikhlinin A., Kravtsov A. V., 2007a, ApJ, 655, 98
Nagai D., Kravtsov A. V., Vikhlinin A., 2007b, ApJ, 668, 1
Nakazawa K., et al., 2009, PASJ, 61, 339
Navarro J. F., Frenk C. S., White S. D. M., 1996, ApJ, 462, 563
Navarro J. F., Frenk C. S., White S. D. M., 1997, ApJ, 490, 493
Oguri M., 2014, MNRAS, 444, 147
Oguri M., Takada M., Okabe N., Smith G. P., 2010, MNRAS, 405, 2215
Oguri M., et al., 2018, PASJ, 70, S20
Okabe N., Smith G. P., 2016, MNRAS, 461, 3794
Okabe N., Umetsu K., 2008, PASJ, 60, 345
Okabe N., Bourdin H., Mazzotta P., Maurogordato S., 2011, ApJ, 741, 116
Okabe N., Smith G. P., Umetsu K., Takada M., Futamase T., 2013, ApJ, 769, L35
Okabe N., et al., 2014a, PASJ, 66, 99
Okabe N., Futamase T., Kajisawa M., Kuroshima R., 2014b, ApJ, 784, 90

Okabe N., Akamatsu H., Kakuwa J., Fujita Y., Zhang Y., Tanaka M., Umetsu K., 2015, PASJ,
Okabe N., et al., 2016, MNRAS, 456, 4475
Okabe N., et al., 2019, PASJ, 71, 79
Pacaud F., et al., 2016, A&A, 592, A2
Pierre M., et al., 2016, A&A, 592, A1
Piffaretti R., Arnaud M., Pratt G. W., Pointecouteau E., Melin J.-B., 2011, A&A, 534, A109
Plagge T. J., et al., 2013, ApJ, 770, 112
Planck Collaboration et al., 2011, A&A, 536, A12
Planck Collaboration et al., 2013, A&A, 550, A131
Planck Collaboration et al., 2014, A&A, 571, A29
Pompei E., et al., 2016, A&A, 592, A6
Poole G. B., Babul A., McCarthy I. G., Fardal M. A., Bildfell C. J., Quinn T., Mahdavi A., 2007, MNRAS, 380, 437
Pratt G. W., et al., 2010, A&A, 511, A85
Pratt G. W., Arnaud M., Biviano A., Eckert D., Ettori S., Nagai D., Okabe N., Reiprich T. H., 2019, Space Sci. Rev., 215, 25
Ricker P. M., Sarazin C. L., 2001, ApJ, 561, 621
Romero C. E., et al., 2015, ApJ, 807, 121
Romero C. E., et al., 2017, ApJ, 838, 86
Romero C. E., et al., 2019, arXiv e-prints, p. arXiv:1908.09200
Rossetti M., Gastaldello F., Eckert D., Della Torre M., Pantiri G., Cazzoletti P., Molendi S., 2017, MNRAS, 468, 1917
Rozo E., et al., 2016, MNRAS, 461, 1431
Rumsey C., Perrott Y. C., Olamaie M., Saunders R. D. E., Hobson M. P., Stroe A., Schammel M. P., Grainge K. J. B., 2017, Monthly Notices of the Royal Astronomical Society, 470, 4638
Ruppin F., et al., 2019, arXiv e-prints, p. arXiv:1911.00560
Rykoff E. S., et al., 2014, ApJ, 785, 104
Rykoff E. S., et al., 2016, ApJS, 224, 1
Sarazin C. L., 1999, ApJ, 520, 529
Schneider P., van Waerbeke L., Jain B., Kruse G., 1998, MNRAS, 296, 873
Sereno M., 2019, ApJ
Sifón C., et al., 2016, MNRAS, 461, 248
Smith G. P., et al., 2016, MNRAS, 456, L74
Smolčić V., et al., 2018, A&A, 620, A14
Soker N., 2016, New A Rev., 75, 1
Tanaka M., et al., 2018, PASJ, 70, S9
Ueda S., et al., 2018, ApJ, 866, 48
Umetsu K., Zitrin A., Gruen D., Merten J., Donahue M., Postman M., 2016, ApJ, 821, 116
Umetsu K., et al., 2019, arXiv e-prints, p. arXiv:1909.10524
Vazza F., Roediger E., Brüggen M., 2012, A&A, 544, A103
Vazza F., Brüggen M., Wittor D., Gheller C., Eckert D., Stubbe M., 2016, MNRAS, 459, 70
Vogt C., Enßlin T. A., 2003, A&A, 412, 373
Voit G. M., Kay S. T., Bryan G. L., 2005, MNRAS, 364, 909
Wik D. R., Sarazin C. L., Ricker P. M., Rand all S. W., 2008, ApJ, 680, 17
Yu L., Nelson K., Nagai D., 2015, ApJ, 807, 12
ZuHone J. A., 2011, ApJ, 728, 54
ZuHone J. A., Markevitch M., Johnson R. E., 2010, ApJ, 717, 908
ZuHone J. A., Kowalik K., Öhman E., Lau E., Nagai D., 2018, ApJS, 234, 4
van Weeren R. J., Röttgering H. J. A., Brüggen M., Hoeft M., 2010, Science, 330, 347
van Weeren R. J., Brüggen M., Röttgering H. J. A., Hoeft M., Nuza S. E., Intema H. T., 2011, A&A, 533, A35

This paper has been typeset from a TEX/LATEX file prepared by the author.